nature portfolio

https://doi.org/10.1038/s41586-025-09044-5

Supplementary information

Integrated photonic source of Gottesman–Kitaev–Preskill qubits

In the format provided by the
authors and unedited

Supplementary Information for
Integrated photonic source of Gottesman-Kitaev-Preskill qubits

M. V. Larsen, J. E. Bourassa, S. Kocsis, J. F. Tasker, R. S. Chadwick, C. González-Arciniegas, J. Hastrup, C. E. Lopetegui-González, F. M. Miatto, A. Motamedi, R. Noro, G. Roeland, R. Baby, H. Chen, P. Contu, I. Di Luch, C. Drago, M. Giesbrecht, T. Grainge, I. Krasnokutska, M. Menotti, B. Morrison, C. Puviraj, K. Rezaei Shad, B. Hussain, J. McMahon, J. E. Ortmann, M. J. Collins, C. Ma, D. S. Phillips, M. Seymour, Q. Y. Tang, B. Yang, Z. Vernon, R. N. Alexander, D. H. Mahler

Xanadu Quantum Technologies Inc., Toronto, Ontario, Canada

(Dated: April 11, 2025)

CONTENTS

I. Experiment 2
A. Experimental setup 2
1. Laser lock system 4
2. Chip 5
3. Homodyne detector 7
B. Mode tomography 7
C. Quadrature squeezing 9
D. State heralding and tomography 10
E. Loss budget 13

II. Photonic chip fabrication, testing, and design 15
A. Fabrication 15
B. Squeezer 15
C. Beamsplitter 16
D. Edge coupler 16
E. Packaging 16

III. Photon Number Resolving Detectors 17

IV. Theory 18
A. GBS architecture and simulation 18
B. Effective squeezing for Gaussian pure states 20
C. Effective squeezing vs. stellar rank 20

References 21

A. Heralded state zoo 23

I. EXPERIMENT

In this section the experimental setup is described in detail, followed by presentation of temporal mode tomography, measured squeezing, state tomography of heralded states, and a loss budget of the experiment.

A. Experimental setup

A schematic of the experimental setup is shown in Fig. S1. Continuous wave light is prepared in the laser lock system described in sec. I A 1. The setup includes 5 sources of light: Local oscillator (LO) at 1553.80 nm wavelength within the dense wavelength division multiplexing (DWDM) band +29; "blue" pump (P1) at 1548.98 nm corresponding to DWDM band +35, approximately 600 GHz blue of the LO; "red" pump (P2) at 1558.64 nm corresponding to DWDM band +23, approximately 600 GHz red of the LO; reference light (Ref), used for phase locking, at 1550.45 nm at DWDM band +35; and probe light (Pr), used the stabilizing resonators, at 1552.19 nm corresponding to DWDM band +31.

LO, P1, P2, and Ref light are carved into pulses using amplitude modulators (AM) (Exail MXER-LN-20-00-P-P-FA-FA-40dB). P1 and P2 are modulated into pulses of 0.5 ns duration (estimated by simulation to be optimal for squeezing generation) with 2 MHz repetition rate. The LO is modulated into alternating 25 ns pulses (used for LO shaping at the homodyne detector) and 5 ns pulses used for phase locking, repeating at 1 MHz, and is aligned in time such that the 5 ns pulse overlaps with every second pump pulse, while the 25 ns pulse is generated 1 ns after every other pump pulse. The 5 ns LO pulse, and corresponding pump pulses, is used for phase locking as described below (and following [1]), while the 25 ns LO pulse is used for homodyne detection. By preventing overlap between the 25 ns LO pulse and every second pump pulse, we prevent distortion by in-fiber FWM of LO and pump pulses used for squeezing generation and homodyne detection. Ref is modulated into 20 ns pulses with 100 kHz

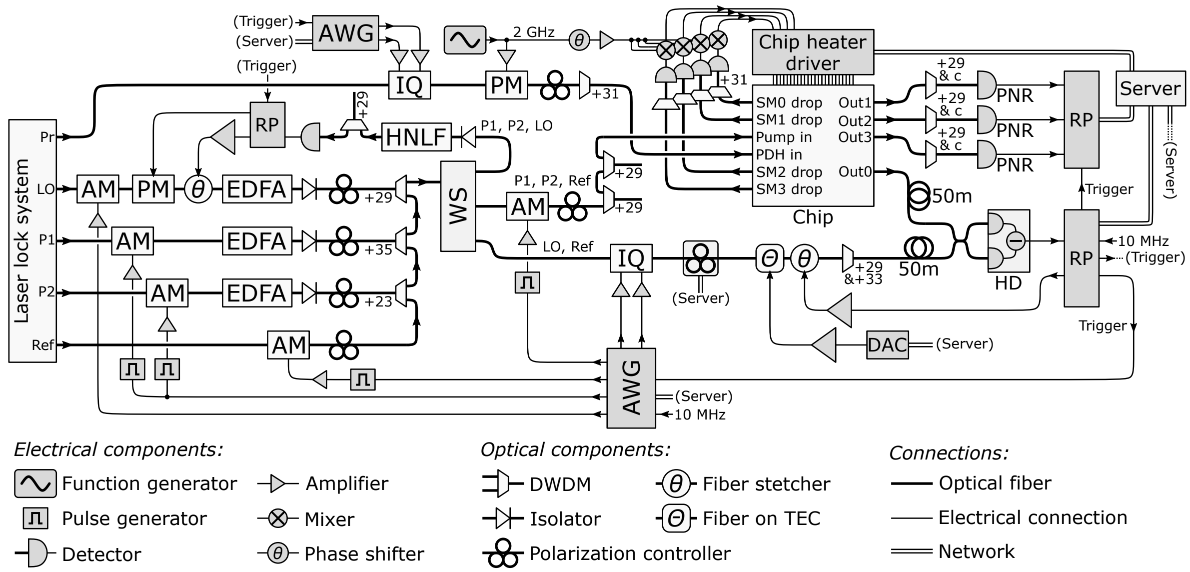

FIG. S1: Experimental setup schematic. Schematic of the laser lock system is shown in Fig. S2, while schematic of the chip is shown in Fig. S3. Acronyms: Electro-optic amplitude modulator (AM), electro-optic phase modulator (PM), electro-optic I/Q modulator (IQ), erbium-doped fiber amplifier (EDFA), highly nonlinear fiber (HNLF), waveshaper (WS), fiber stretcher (θ), fiber coiled on a thermoelectric cooler (Θ), homodyne detector (HD), photon number resolving detector (PNR), RedPitaya (RP), arbitary waveform generator (AWG), digital-analog converter (DAC).

repetition rate. The LO, P1 and P2 pulses are amplified using erbium-doped fiber amplifiers (EDFA) (P1/P2: Pritel LNHGFA-20, LO: Pritel LNHGFA-33). The pump is amplified to produce pulses of 300–400 pJ energy in each pump pulse at each of the 4 on-chip squeezers (discussed later). The LO is amplified to maximize electronic noise clearance in the homodyne detection (discussed later). Finally, P1, P2 and LO are combined in one fiber together with Ref using a network of DWDM filters and sent to the input of a waveshaper (Finisar 4000A). Using the waveshaper, light at different wavelengths are divided between the waveshaper's output ports.

To stabilize the phase between LO, P1 and P2 at the point of the waveshaper, 4% of the LO, and 0.2% of each P1 and P2 is output on one of the waveshapers output ports and sent through a highly nonlinear fiber (Sumitomo OCL2021-087). The phase of the squeezing generated on chip via four-wave mixing (FWM) depends on the pump phase as $(\phi_{\mathrm{P1}} + \phi_{\mathrm{P2}})/2$, where $\phi_{\mathrm{P1(2)}}$ is the phase of P1(2). Thus we wish to stabilize $(\phi_{\mathrm{P1}} + \phi_{\mathrm{P2}})/2$ relative to the LO phase, ϕ_{LO}. In the HNLF, every second pump pulse pair overlapping with the 5 ns LO pulse experiences gain by FWM depending on $(\phi_{\mathrm{P1}} + \phi_{\mathrm{P2}})/2 - \phi_{\mathrm{LO}}$. We detect the amplified pumps (after filtering off the LO using a DWDM) using a photodetector (Thorlabs PDA05CF2), and use the measured amplification to feed back to a fiber stretcher (Optiphase PZ1-SMF4-APC-E) in the LO path to stabilize $(\phi_{\mathrm{P1}} + \phi_{\mathrm{P2}})/2 - \phi_{\mathrm{LO}}$. This is done using a dither lock scheme implemented with a RedPitaya (RP)(STEMlab 125-14) phase modulating the LO path at 500 kHz using an electro-optic phase modulator (PM) (Exail MPZ-LN-01). The signal fed back to the fiber stretcher is amplified using a high-voltage amplifier (PiezoDrive PX200).

On a second output port of the waveshaper, we output the remaining P1 and P2, and half of the Ref. Using an AM, the 2 MHz pump repetition rate is reduced to 200 kHz, determined by the bandwidth of the photon number resolving (PNR) detection system. In a 10 µs period, the AM lets through two pump pulses which have not overlapped in time with an LO pulse, and the Ref pulse. The light is reflected on two channel +29 DWDMs to remove noise photons at the squeezing wavelength (from e.g. Raman, FWM, etc.) before being sent to the pump input of the chip. The chip is described in sec. I A 2. Three of the four chip outputs are sent to three photon number resolving (PNR) detectors. Before PNR detection, photons outside the squeezing band are filtered using custom DWDM filters from Opneti, centered at DWDM band +29, but with an extended rejection band rejecting light from 1194 nm to 1715 nm wavelength and low insertion loss of 0.231–0.283 dB. The remaining chip output is sent to the signal input of the homodyne detection system. All fiber paths between chip and detectors are fully fusion spliced.

On the third output port of the waveshaper, we output LO and the second half of Ref. Here the temporal LO profile used for pulsed homodyne detection is shaped from the 25 ns LO pulse using an I/Q modulator (IQ) (Exail MXIQER-LN-30). The profile is chosen to match the measured squeezing temporal mode profile described in sec. I B. The shaped LO pulse is prepared at a 1 MHz repetition rate. Here, in a 10 µs time period, two of the shaped LO pulses are used for homodyne detection of the generated quantum state, while the remaining eight shaped LO pulses are used for shot-noise calibration of the homodyne detector. The IQ modulator passes the Ref pulse through. To remove any potential noise outside the LO and Ref band, a DWDM filter is used in the LO path before homodyne detection.

While the homodyne detector is engineered for high detection efficiency, it is inevitable that a small fraction of the LO is reflected back to the chip. In the chip, the back-reflected LO is reflected forward again by scattering in the on-chip ring resonators and into the PNR detectors. Due to the photon number resolution, we are very sensitive to any LO reflected into the PNRs. Using a 50 m optical fiber between the chip and the homodyne detector, any reflected LO is delayed by approximately 0.5 µs at the PNR detectors, and we can distinguish reflected LO light from the generated quantum state. To keep the LO pulses and squeezed state aligned in time at the homodyne detector, another 50 m fiber is placed in the LO path.

The interferometer between the waveshaper and the homodyne detector, formed by the chip path and the LO path, is imbalanced by 9 ns in order to overlap the generated quantum light from the chip with shaped LO pulse (note, the initial 25 ns LO pulse was displaced 1 ns in time compared to the corresponding pump pulse to prevent distortion due to in-fiber FWM between LO and pumps before the waveshaper). The interferometer is phase stabilized using the Ref interfering at the homodyne detector (note, the Ref pulse is longer than the interferometer imbalance). The interference is fed back using an RP to a fiber stretcher (General Photonics FPS-003), driven with a high-voltage amplifier (PiezoDrive PX200). Since the interferometer is imbalanced and the Ref is at a different wavelength from the LO and quantum light, any re-lock of the phase stabilization causes a random offset between the phase of the LO and the quantum light. Hence, to prevent re-locks, several meters of the fiber in the LO path is coiled on a thermoelectric cooler (TEC). Using the TEC to cool or heat the fiber allows a long phase locking range: during phase locking the fiber stretcher is kept in range by controlling the TEC temperature typically allowing >12 hours uninterrupted phase stabilization.

Primarily single mode (SM) non-polarization maintaining fiber is used in the experiment. Manual polarization controllers (Thorlabs FPC562) are used to control and align polarizatons, except in the LO path where an electronic polarization controller (BATI PCM400) is used, allowing automated optimization of the LO polarization using the quantum light output from the chip. Electro-optical modulators (AM, PM and IQ) use polarization maintaining fibers, so polarization controllers and polarization beamsplitters are used to couple into the modulators. To bias lock AM and IQ modulators, 1% and 10%, respectively, are tapped off from the modulators' outputs, detected, and fed back using RPs to the modulators' DC bias ports.

The homodyne detection output is acquired using the same RP used for phase stabilizing the LO path. The PNR detection is acquired using a 4 channel RP (STEMlab 12-14 4-input), triggered from the homodyne detection acquisition RP. The RPs are running with a custom FPGA image developed within Xanadu allowing real-time analysis of PNR detector and HD time traces. For each homodyne and PNR measurement, a quadrature value and 3 photon number outcomes are sent to a server where they are sorted by photon number and stored. Due to noise, each photon number output from the PNR detectors are accompanied by a confidence value which we store and use in the data analysis to discard the most noisy data.

The RP used for homodyne detection acquisition is used to trigger the pulse generation throughout the experiment by triggering an arbitrary waveform generator (AWG) (Keysight M8190A). The two analog outputs of the AWG are used for LO shaping by driving the RF input ports of the IQ modulator after amplification using (Exail DR-VE-10-MO) amplifiers. Digital AWG outputs are used to trigger pulse generators (Highland Technologies T240) driving AMs through amplifiers (Exail DR-VE-10-MO)(except the AM in the LO path which is driven without using a pulse generator). All timing-related electronics (RPs and AWGs) receive a 10 MHz tone from a central Rubidium clock source (SRS FS725/2) for synchronization purposes.

Finally, the Pr light is used for stabilizing on-chip resonators via the Pound–Drever–Hall (PDH) locking technique [2]. The Pr light is pulsed using an IQ modulator allowing frequency shifting the Pr pulses, and further phase modulated at 2 GHz using a PM. The pulsed Pr is sent to the chip where it is distributed and interacts with four ring resonators before it is coupled out of the chip again into four fibers, one for each resonator, and detected. The detected signal is mixed with the 2 GHz modulation tone, and naturally low-pass filtered by the bandwidth of the following electronics, to generate a PDH error signal used for feedback to the ring resonators' thermo-optic heaters, stabilizing their resonance frequency to the Pr pulses. All thermo-optic heaters on the chip are controlled by a custom designed current driving circuit.

1. *Laser lock system*

A schematic of the laser lock system is shown in Fig. S2. 10% of the optical power from all five lasers in the experiment is tapped off, and the remaining power is sent to the rest of the optical circuit. All lasers have optical isolators at their outputs to prevent back-reflections. In the case of the LO laser, the tap-off is used to generate an optical frequency comb (OFC) that serves as the frequency and phase reference for the experiment. The tap-offs of the other lasers are used to lock them to the OFC. The tapped-off light from P1, P2, Ref and Pr is sent into SM fiber, but since this light interferes with the OFC, manual polarization controllers (Thorlabs FPC562) are added in these paths to align polarizations.

The LO laser (Oewaves OE4023), P1 and P2 lasers (TOPTICA CTL1550) are continuous-wave lasers with polarization-maintaining fiber outputs. The 10% tap-off from the LO is sent through two

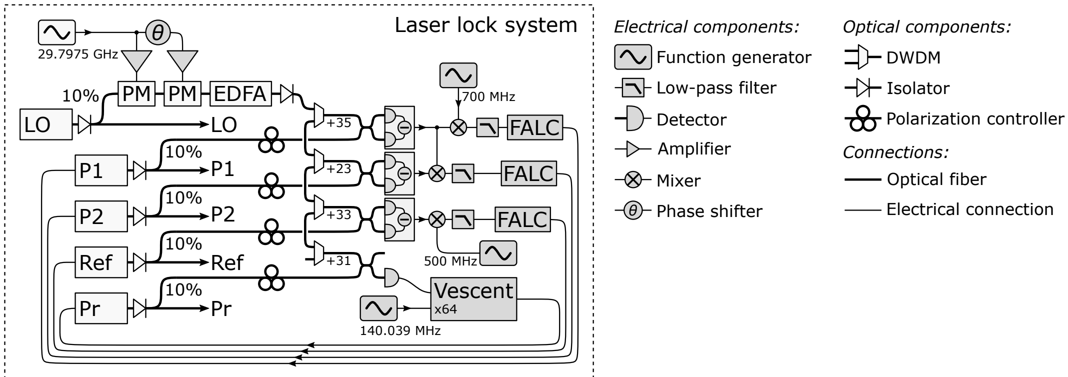

FIG. S2: Laser lock system schematic. Acronyms: Electro-optic phase modulator (PM), erbium-doped fiber amplifier (EDFA).

consecutive PMs (EOspace PM-5VEK-40-PFA-PFA-UV-UL) to deeply modulate the phase of the light. The PMs are driven by a microwave synthesizer (Signalcore SC5521A), whose output is split and sent through two microwave amplifiers (RF-lambda RFLUPA26G40GA) with a microwave phase-shifter (Pasternack PE82P1000) in between them, ensuring that the two PMs modulate the light in-phase to achieve maximum width of the OFC. After the second PM, the 10% LO light is sent through an EDFA (Amonics AEDFA-33-B-FA) to increase the power of the OFC enough for stable phase locking.

The optical frequency comb has a tooth spacing off 29.7975 GHz, set by the output of the microwave synthesizer, and spans more than 1.2 THz comprising more than 25 comb teeth on each side of the LO. P1 is tapped off to interfere with the OFC at a 700 MHz blue-detuned sideband from the 20th tooth. The beatnote is detected on a balanced detector (Wieserlab WL-BPD1GA), and the subtracted photocurrent is mixed (MiniCircuits ZX05-10L-S+) with a 700 MHz reference tone generated from an external synthesizer (Valon 5009a). After low-pass filtering (MiniCircuits VLF-160+), the error signal is sent to a fast PID locking module (TOPTICA FALC pro & DLC pro) to lock the frequency and phase of P1 to the comb tooth. A *transfer-oscillator lock* is used for P2, meaning that its reference tone is the beatnote between P1 and corresponding comb tooth. The P2 laser is locked to the symmetric 20th tooth red-detuned from the OFC carrier, and hence any "breathing-mode" noise of the OFC should have a highly correlated effect on P1 and P2. The experiment is insensitive to anti-correlated phase/frequency noise in P1 and P2 of this kind since only the phase $(\phi_{\mathrm{P1}}+\phi_{\mathrm{P2}})/2$ affects the squeezing generation.

The Ref laser (TOPTICA DL pro) and Pr laser (IDPhotonics Co-Brite) generate the light denoted "Locks" at the chip input in Fig. 2 of the main text. The reference laser is locked at 500 MHz offset to the 14th OFC tooth between the LO and P1, using another externally generated RF tone (Valon 5009a) and a PID locking module (TOPTICA FALC pro & DLC pro). The frequency of this laser is chosen so that a significant fraction of its power can pass through the chip filters, while also being far from any on-chip ring resonances. The Pr laser is locked to the 7th OFC tooth between the LO and P1, but its frequency is chosen to align with a ring resonance. The Pr laser generates a beatnote close to 9 GHz with the 7th OFC tooth, and is locked using another PID controller (Vescent DC-125). This PID servo controller has an internal $\times 64$ multiplier for the external reference tone, as well as an internal RF mixer.

All external function generators used in laser locking were synchronized to the 10 MHz tone of the central Rubidium clock source. This ensures long-term stability of all electronically-generated signals.

2. Chip

Fig. S3 shows a functional schematic of the packaged chip. Pump light is input to the chip through fiber *Pump in*. The input pump light is filtered by an asymmetric Mach-Zehnder interferometer (MZI),

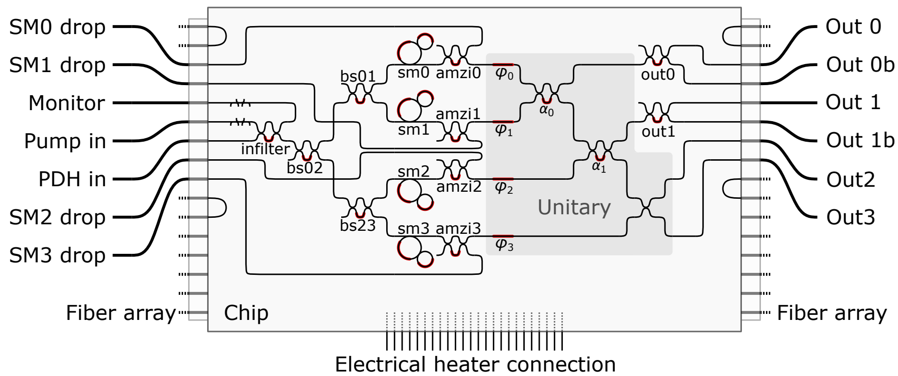

FIG. S3: Functional chip schematic. The schematic shows the photonic integrated circuit and the edge coupling via fiber arrays. Red lines symbolize thermo-optic phase shifters.

infilter, with 1.2 THz free spectral range (FSR) passing P1 and P2 but further filtering noise photons at the squeezing wavelength. Part of Ref is lost in *infilter* due to the filter being optimized to pass P1 and P2.

Using MZIs labelled *bs02*, *bs01*, and *bs23*, light is distributed to four squeezers, *sm0–3*, to generate 10 dB of squeezing (before loss) in *sm0* and *sm1*, and 8 dB of squeezing (before loss) in *sm2* and *sm3*. The squeezers consist of two coupled ring resonators: A primary resonator, which we will refer to as the "body" resonator, of 200 GHz FSR, coupled to the bus wave guide, and tuned for P1 and P2 to be on resonance for squeezing generation in a resonance centered between the P1 and P2 resonances; and an auxiliary resontator, which we will refer to as the "head" resonator, of $4/3 \times 200$ GHz FSR coupled to the body resonator forming a two-resonator photonic molecule design which we refer to as a "snowman" (described further in sec. II B) [3]. The function of the head resonator is to split and displace body resonances 1.2 THz from the signal resonance suppressing non-degenerate spontaneous four-wave mixing and allowing for only degenerate squeezing generation in the signal resonance centered between the two pump resonances (to first order approximation). The signal resonances of the body resonators, in which squeezing is generated, are measured to have an average full width at half maximum bandwidth of 580 ± 2 MHz and $97.4 \pm 0.10\%$ escape efficiency corresponding to a loaded and intrinsic quality factor of $(333 \pm 8) \times 10^3$ and $(12.8 \pm 0.7) \times 10^6$, respectively.

After squeezing generation, the pump light is filtered off using asymmetric MZIs (*amzi0–3*) of 400 GHz FSR before the squeezing enters the programmable linear network, or unitary. The filtered pump light is guided off the chip, collected in fibers *SM0–3 drop* and detected for monitoring purposes.

The pulsed Pr light used for PDH locking of the snowmen body resonators is coupled into the chip through the *PDH in* fiber. A portion of the Pr light is lost in the *infilter* before being distributed to each *sm0–3*. After interacting with *sm0–3*, the Pr light is filtered out together with the pumps and detected for feed back control of the thermo-optic phase shifters on the snowmen body resonators. While the pumps are coupled into the snowmen at 3 body FSRs away from the squeezing resonance, Pr is coupled to a body resonance 1 FSR away from the squeezing resonance on the blue-detuned side. The head resonances are not actively stabilized.

After *amzi0–3* the squeezing enters the unitary consisting of 4 thermo-optic phase shifters ($\phi_0, \phi_1, \phi_2, \phi_3$), 2 variable beamsplitters, each consisting of an MZI with a thermo-optic phase shifter, (α_0, α_1), and one fixed beamsplitter of 50:50 splitting ratio. The arrangement is shown in Fig. S3, and is referred to as a "staircase" unitary. The parameters α_0 and α_1 are optimized by measuring the mean photon number in the PNR detectors on the chip outputs as a function of α_0 and α_1. ϕ_0, ϕ_1, ϕ_2, and ϕ_3 are optimized by using the PNR detectors to measure second-order coherence functions between different chip output modes as function of α_0, α_1, ϕ_0, ϕ_1, ϕ_2, and ϕ_3, enabling squeezers (by engaging the PDH lock) two at a time. The settings used for the states heralded and presented in Fig. 3 of the main text are

$$(\alpha_0, \alpha_1) = (2\theta, 2t) \quad , \quad (\phi_0, \phi_1, \phi_2, \phi_3) = (-\theta, -\theta, -\pi/2, t) \; , \tag{1}$$

where

$$t = \arctan\sqrt{2} \quad , \quad \theta = 0.58\,. \tag{2}$$

Here $\alpha_0 = 2 \times 0.58$ correspond to 70.0% transmission from *sm0* to *out0*, and $\alpha_1 = 2t$ correspond to 66.6% transmission from *sm2* to *out1*. The corresponding circuit diagram is shown in Fig. S17 of sec. IV A.

Due to finite extinction of the *amzi0–3* filters, part of the pump pulses leaks through the unitary and out of the chips main outputs. For the PNR detection, the leaked pump pulses are caught by the DWDM filters before PNR detectors. For the homodyne detection however, the pump light leads to degradation of the homodyne clearance, as the pump pulses function as an effective unwanted local oscillator adding shot noise at the pump wavelength. To prevent this, a final MZI filter, *out0*, of 400 GHz FSR is used before the spatial mode going to the homodyne detector is coupled off the chip. Another similar filter *out1* is placed in the second spatial mode allowing the chip to be reconfigured to be operated as a 3-mode chip with the homodyne detector connected to fiber *Out1* instead of fiber *Out0*.

3. Homodyne detector

The homodyne detector consists of a balanced fiber beamsplitter coupled to two 100 µm diameter photodiodes (Laser Components IGHQEX0080) using anti-reflection coated graded index (GRIN) lenses coupling light from fiber onto the photodiodes. The subtraction photocurrent of the photodiodes is amplified by a custom-built transimpedance amplifier (TIA) circuit with a 3 dB bandwidth of approximately 10 MHz. To achieve low noise, the TIA circuit uses a low current-noise operational amplifier (Analog Devices LTC6268-10) and a high feedback transimpedance gain (475 kΩ). We measure a maximum shot-noise clearance of 21.3 dB with 17.1 pJ LO pulse energy.

B. Mode tomography

To measure the temporal mode profile of the generated state, and to estimate how close to being single mode the squeezing generation is, we perform mode tomography: Each snowman squeezer is activated independently (by shifting the body resonance frequency of all other snowmen so that pump does not couple into them), and a chip output is connected to a continuous wave heterodyne detector. The heterodyne detector considered here consists of two homodyne detectors measuring $\pi/2$ out of phase, and uses a continuous wave local oscillator. The input light to the detector, a quantum squeezed state, is split in two (thus mixing it with vacuum) and measured on the two homodyne detectors. From the two homodyne detector outcomes, we can reconstruct the N-moment of the quantum field, $N(t_1, t_2) = \langle a^\dagger(t_1) a(t_2)\rangle$, from measured time-dependent quadrature variance and correlations between the homodyne detectors [4]. The N-moment measured from squeezing generated in the first snowman, *sm0*, is shown in Fig. S4. The N-moments measured from squeezing generated in *sm1–3* look very similar.

Diagonalizing the N-moment gives eigenvectors and eigenvalues, which determine the temporal mode profiles and corresponding mean photon numbers, respectively. Fig. S5(left) shows the fundamental temporal mode (mode of largest eigenvalue and thereby largest photon occupation) of each snowman squeezer. The mode amplitude profile is mainly defined by the 0.5 ns pump pulse and the body resonator decay time. The mode phase profile is dominated by self- and cross-phase modulation by FWM between pumps and the squeezing in the ring. The fundamental temporal modes are seen to be close to indistinguishable, and the overlap efficiencies between all modes are $\geq 99.95\%$. Here we define the overlap efficiency between mode k and n as $\left|\int f_k(t) f_n^*(t)\,\mathrm{d}t\right|^2$ where $f_k(t)$ is the complex temporal mode profile of mode k.

Fig. S5(right panel) shows the absolute eigenvalues for all temporal modes. The eigenvalues are sorted from highest to lowest and values to the right of the plotted minimum are negative. Note,

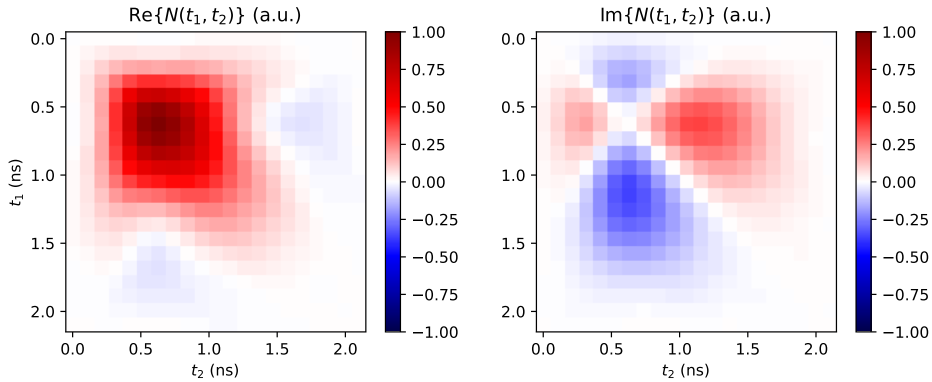

FIG. S4: *N*-moment of generated squeezing. The N-moment is measured by continuous wave heterodyne detection from the first snowman squeezer, *sm0*.

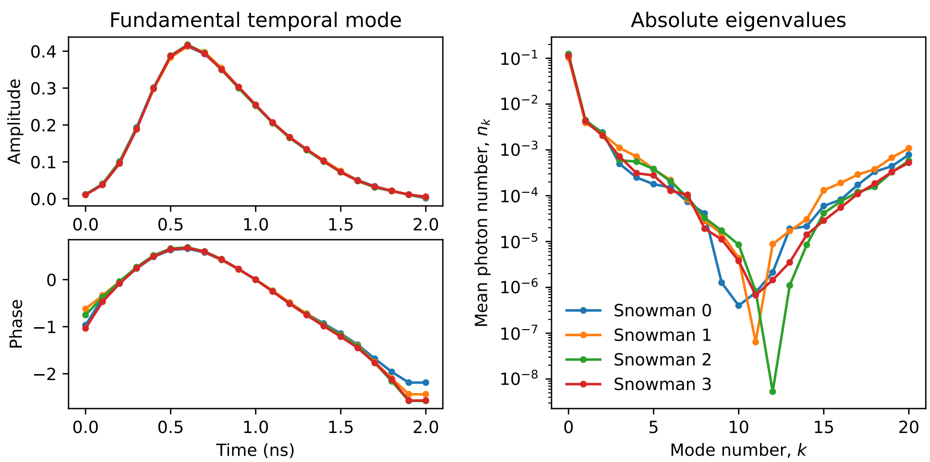

FIG. S5: Temporal modes of generated squeezing. (left) shows the fundamental temporal mode (eigenvector of largest eigenvalue) of each squeezer. (right) shows the absolute value of the eigenvalues of the N-moment, corresponding to the mean photon number in each temporal mode.

due to the number of data points used in the construction of the N-moment, the eigenvalues are susceptible to spreading due to statistical noise. For example, negative eigenvalues, corresponding to negative mean photon numbers, are not physical. Thus, to estimate the Schmidt number [5] of each squeezer, we define a temporal mode cutoff and only use eigenvalues larger than the spread of statistical noise. Using eigenvalues, n_k, of mode $k = 0$, 1, and 2, the Schmidt number, $K = (\sum_k n_k)^2/\sum_k n_k^2$, of squeezing generated from snowman 0, 1, 2, and 3 is estimated to be 1.116, 1.121, 1.110 and 1.112, respectively. Note that our estimate for the Schmidt number would increase if the cutoff were increased to include smaller eigenvalues, however, in this case the Schmidt number would likely be overestimated.

The measured Schmidt numbers are in good agreement with simulation of the snowman ring structure: From simulation (solving the linear and nonlinear dynamics of the two coupled resonators via time domain coupled mode theory), with the used pump pulse profile (0.5 ns square pulses) and coupling to the snowman ring structure, we expect Schmidt number around $K \sim 1.1$. The Schmidt number can potentially be lowered by using interferometric coupling to the ring structure [6], or more advanced pump profiles [7]. Simulation of the state preparation is shown in Fig. S18 of section IV A when including and excluding the effect of Schmidt number $K \sim 1.1$.

The mode tomography performed here is carried out with approximately 10 dB squeezing generated

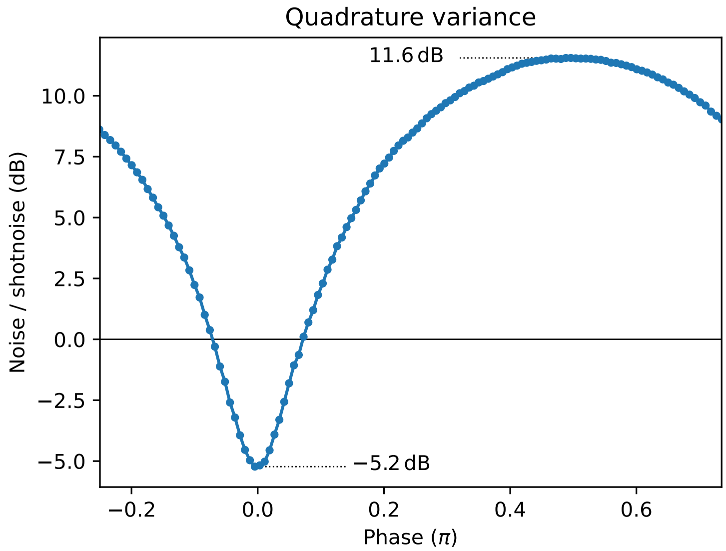

FIG. S6: Measured squeezing. Quadrature variance as a function relative phase between squeezed state and local oscillator.

from each snowman (before loss). However, for GKP-state generation, we desire that two of the snowmen only produce 8 dB of squeezing, which is achieved by using less pump power in those snowmen. With less pump power coupled into the snowman body resonator, we can expect the temporal mode to deviate slightly in its phase profile. Nevertheless, from simulations we expect 99% overlap efficiency between temporal modes of 8 dB and 10 dB squeezing generation, while we expect the Schmidt number to change by less than 0.011.

C. Quadrature squeezing

We prepare a squeezed state at the homodyne detector by setting $\alpha_0 = 0$, by which the first MZI in the chip staircase unitary equals an identity gate and passes squeezing from the first snowman to *Out0*, which is connected to the homodyne detector. Fig. S6 shows the measured quadrature variance as a function of relative phase between the squeezed state and LO when optimizing the pump power for maximum measured squeezing.

We measure up to 5.2 dB of squeezing and 11.6 dB of anti-squeezing. Assuming the generated squeezed state to initially be a pure squeezed state before loss is applied, and when compensating for 2.1° standard deviation phase noise, the measured squeezing and anti-squeezing would correspond to an initial pure squeezed state of 12.7 dB squeezing and 76.0% overall efficiency from squeezing generation to detection. However, this is an underestimation of the actual overall efficiency, and can be considered a lower bound: Due to parasitic FWM in the snowman structure, we do not initially generate a pure squeezed state in the ring resonator's squeezing mode, but rather a state entangled in the quadratures to other resonance modes. Since, in the current experimental implementation, we only perform measurements (PNR and homodyne detection) of modes corresponding to the squeezing resonance mode, the resulting measured state appears as a squeezed thermal state when tracing out all other resonance modes. A squeezed thermal state can be parameterized as a squeezed vacuum state of additional squeezing followed by additional loss. Since we cannot distinguish the squeezed thermal state from a squeezed vacuum state with extra squeezing and loss, the actual initial squeezing, when including parasitic FWM process, will be less than the estimated initial squeezing when ignoring parasitic FWM process, and the actual efficiency must be higher.

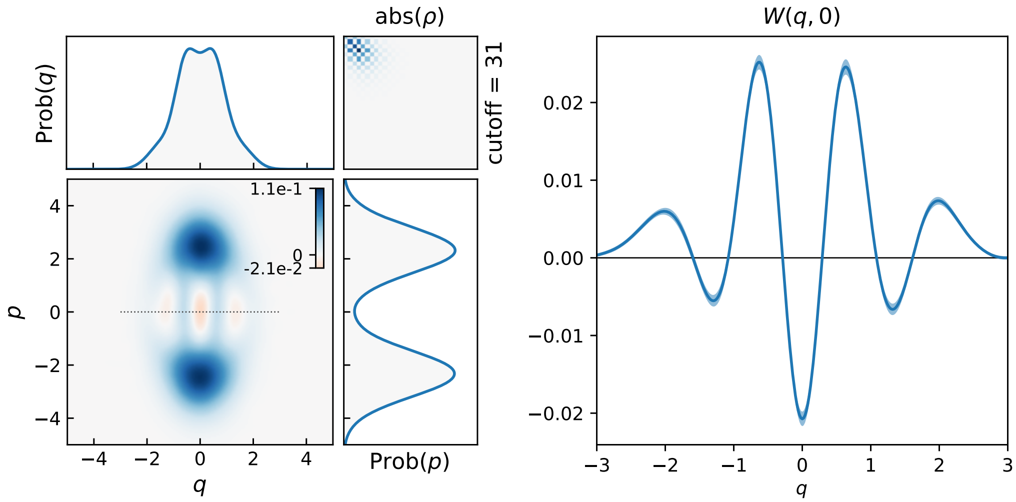

FIG. S7: State tomography result of the (1,1,1)-state. Left panel shows the state Wigner function, quadrature probability distributions, and absolute value of the density matrix. Uncertainties of the quadrature probability distributions are smaller than the plotted line width. Right panel shows a cut through the Wigner function, marked with a dotted line in the left panel. The light blue area correspond to the uncertainty estimated by bootstrapping.

Possible parasitic FWM processes include the non-degenerate spontaneous FWM suppressed by resonance splittings using the head resonator, as well as higher order parasitic FWM processes enabled by a comb generated in the body resonator from stimulated FWM of the two pump fields. The comb generated with 1.2 THz teeth spacing allows new non-degenerate spontaneous FWM processes to generate entanglement between the squeezing resonance and other resonance modes causing thermalization effects when tracing out those modes. From simulation, we estimate the comb enabled higher order parasitic FWM processes to dominate the thermalization effect of our squeezing.

D. State heralding and tomography

For state tomography, data was acquired over 12.8×10^9 repetitions of the experiment running at 200 kHz repetition rate, corresponding to approximately 18.5 hours of data acquisition when including time overhead in storing data and updating the LO phase for quadrature measurements at different phases. Acquired data includes quadrature measurements sorted by the photon number outcomes from the PNR detectors, as well as a corresponding confidence value of each PNR detector outcome. To reduce photon number outcomes affected by noise in the PNR detector, or by light leaked into the PNR detectors at different times than our quantum state (e.g. reflected LO), we start by discarding 20% of the data with lowest confidence leading to a reduction of data by a factor $(1 - 0.2)^3 \approx 0.5$. We then reconstruct the density matrix from the remaining quadratures using maximum-likelihood techniques [8]. The Wigner functions of all quantum states heralded with $(n_1 \leq 5, n_2 \leq 5, n_3 \leq 5)$ are shown in Appendix A. Below we present a subset of the most interesting heralded and reconstructed states with $n_1 + n_2 + n_3 \leq 12$, where the heralding probability is high enough to warrant statistical significance of the reconstructed state. All states are presented using $\hbar = 1$.

Uncertainties are estimated by bootstrapping where we create 100 new data sets by resampling the original data set with replacement. For each of the 100 new data sets we reconstruct a density matrix from which a figure-of-merit of interest is calculated. The corresponding uncertainty is estimated as the standard deviation of this figure-of-merit calculated from each of the 100 data sets.

Fig. S7 shows the state heralded from the $(n_1, n_2, n_3) = (1, 1, 1)$ PNR detection pattern. The state

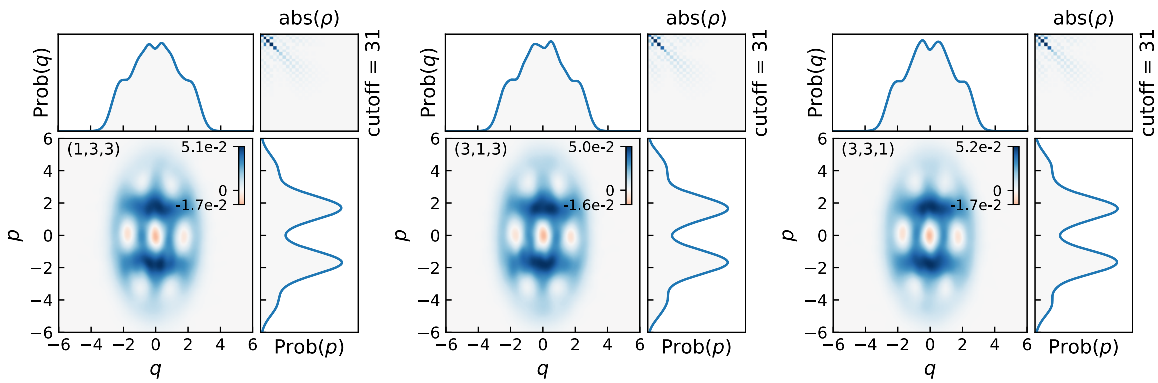

FIG. S8: State tomography results of (1,3,3), (3,1,3). and (3,3,1) states. For each state the Wigner functions, quadrature probability distributions and absolute value of the density matrix are shown.

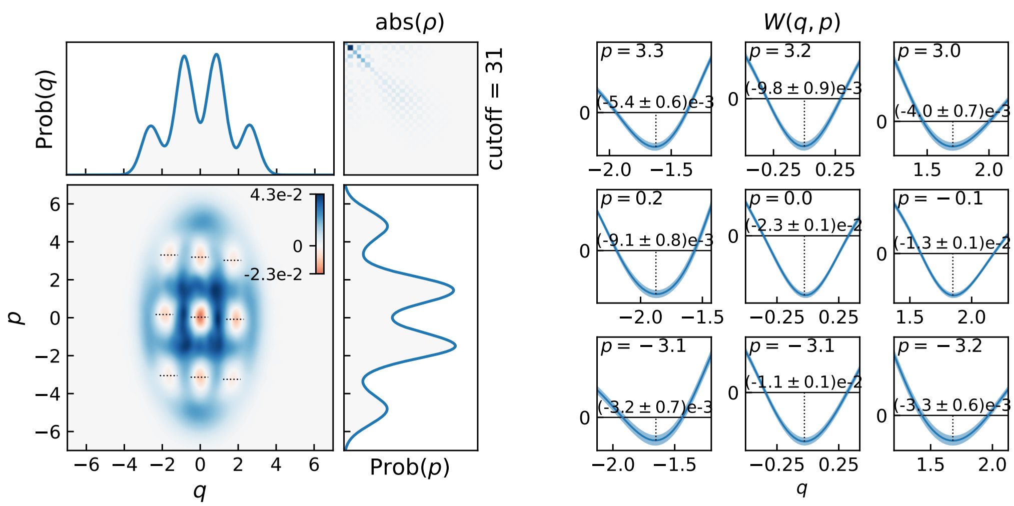

FIG. S9: State tomography result of the (3,3,3)-state. (left) shows the Wigner function, quadrature probability distributions and absolute value of the density matrix. (right) shows cuts through the Wigner function as marked with dotted lines in (left). The light blue area correspond to the uncertainty estimated by bootstrapping.

is heralded with a success probability of 1.69×10^{-2} before discarding PNR detection data. The state is reconstructed using 2 000 000 quadrature measurements. The state resembles a cat state with 3 negative fringes as shown in Fig. S7(right).

Fig. S8 shows the three states heralded from $(n_1, n_2, n_3) = (1, 3, 3)$, $(3, 1, 3)$, and $(3, 3, 1)$ heralding events, which are heralded with success probability of 9.02×10^{-4}, 9.19×10^{-4}, and 9.38×10^{-4}, respectively, before discarding PNR detection data. The states are each reconstructed using 2 000 000 quadrature measurements. The states resemble a GKP state with a hexagonal grid.

Fig. S9 shows the state generated from the $(n_1, n_2, n_3) = (3, 3, 3)$ heralding event, and is heralded with success probability of 2.93×10^{-4} before discarding PNR detector data. The state is reconstructed from $\sim$1 800 000 quadrature measurements. The state resembles a GKP state with a rectangular grid. Fig. S9(right) shows cuts through the Wigner function at the $3 + 3 + 3 = 9$ negative regions, by which all 9 regions are shown to be negative (with negativity exceeding beyond uncertainties).

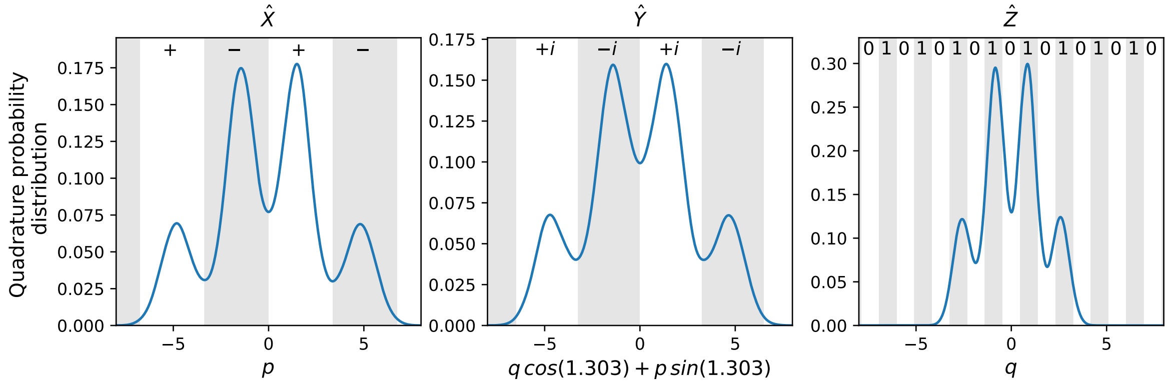

FIG. S10: Quadrature probability distributions that allow us to measure the Pauli operators for the rectangular lattice GKP qubit.

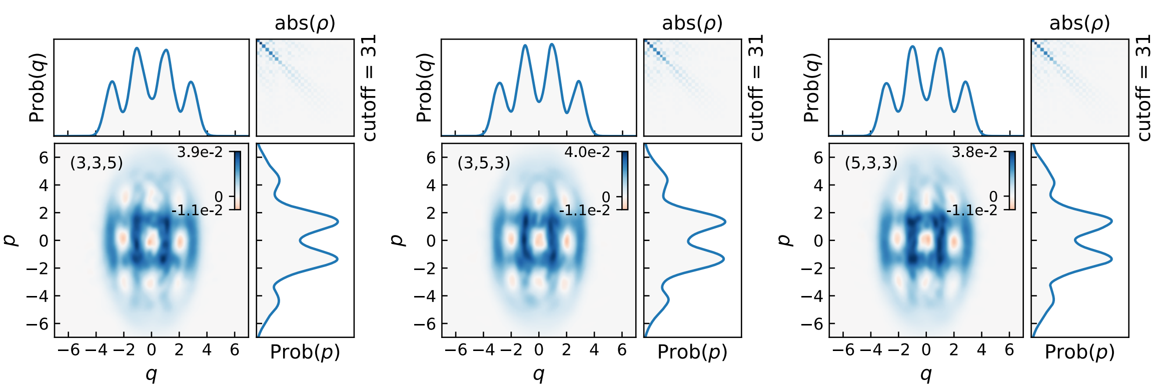

FIG. S11: State tomography results of (3,3,5), (3,5,3). and (5,3,3) states. For each state the Wigner functions, quadrature probability distributions and absolute value of the density matrix is shown.

Fig. S10 shows quadrature probability distributions that allow us to measure the Pauli operators for the rectangular lattice GKP qubit. The Pauli expectation values presented in the main text are calculated by integrating the quadrature probability distributions against the binning functions highlighted in white and gray in the figure.

Fig. S11 shows the three states heralded from $(n_1, n_2, n_3) = (3, 3, 5)$, $(3, 5, 3)$, and $(5, 3, 3)$ heralding events, which are heralded with success probability of 9.24×10^{-5}, 9.50×10^{-5}, and 9.66×10^{-5}, respectively. Each of the states are reconstructed using $\sim$600 000 quadrature measurements. the states resembles a GKP state with rectangular grid, and is similar to the $(3, 3, 3)$-state above but with a different grid aspect ratio.

There are many output states that by construction lie on the same GKP lattice, such as the three states presented in Fig. S11; in the case of uniform loss, they are the same state. To illustrate, in Fig. S12 the combined state (under convex combination) of the $(3, 3, 5)$, $(3, 5, 3)$ and $(5, 3, 3)$ heralding events is shown, which now has a combined success probability of 2.84×10^{-4}. The same is true for other heralding patterns that differ by permutations of (n_1, n_2, n_3) e.g. the states shown in Fig. S8.

Fig. S13 shows the state heralded from the $(n_1, n_2, n_3) = (4, 4, 4)$ heralding event, and is heralded with 5.38×10^{-5} success probability before discarding PNR detector data. The state is reconstructed from just $\sim$300 000 quadrature measurements and thus the Wigner function is noisier than for the other presented states. The right panel of Fig. S13 shows cuts through the Wigner function in the

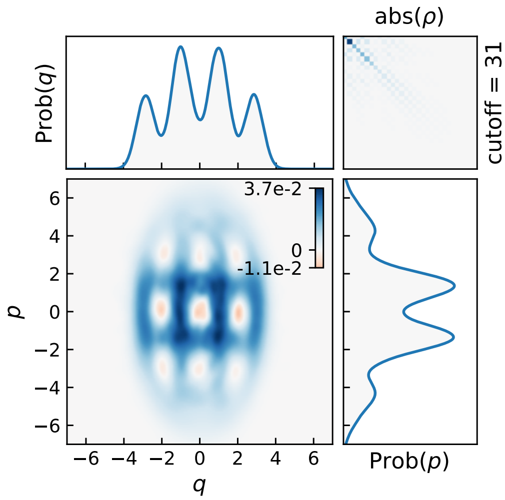

FIG. S12: Combined state of the (3,3,5)-, (3,5,3)-. and (5,3,3)-state. The state is combined as a mixture of the density matrices shown in Fig. S11.

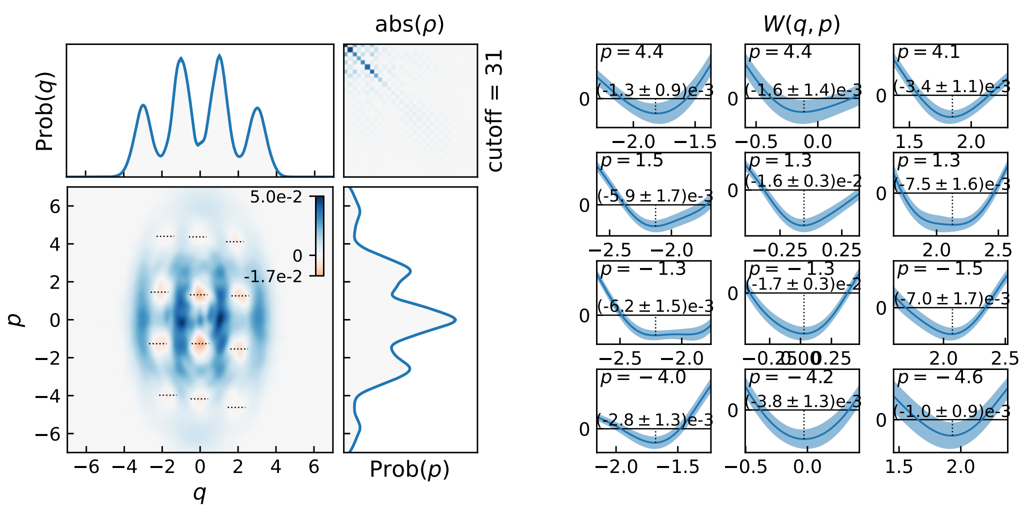

FIG. S13: State tomography result of the (4,4,4)-state. Left panel shows the Wigner function, quadrature probability distributions and absolute value of the density matrix. Right panel shows cuts through the Wigner function as marked with dotted lines in the left panel. The light blue area correspond to the uncertainty estimated by bootstrapping.

$4+4+4 = 12$ regions of negativity. All 12 regions are negative with negativity larger than the standard deviation, albeit only marginally for a few cuts.

E. Loss budget

In this experiment, the total loss experienced by photons generated in the squeezers is of paramount importance—any loss degrades the quality of the heralded state. In the heralding arms, loss degrades

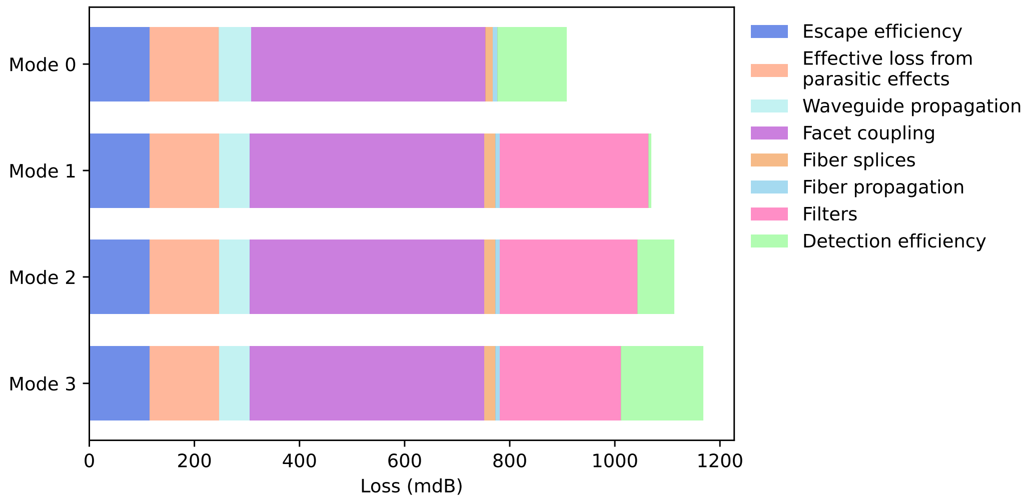

FIG. S14: Loss budget in units of milli-dB (mdB). Mode 0 is the mode that is heralded, and thus reaches the homodyne detector for state tomography. Modes 1, 2 and 3 are the modes sent to PNR detectors for heralding.

the heralded state by allowing the incorrect photon number to herald the production of a state. This is because the states heralded by incorrect photon detection events may not have the same parity as the target state, and thus averaging these states with the target state may "wash out" the regions of negativity so critical to GKP state structure. The "staircase" GBS was designed with this in mind, with the squeezing levels and interferometer tuned so that the support of the multimode Gaussian state in Fock space is such that the probability of (n, n, n) is much greater than $(n, n, n+1)$, $(n+1, n, n)$, and $(n, n+1, n)$, leading to a lower probability that single photon loss events in the heralding arms contaminate the output state (see Fig. S12a of Ref. [9] and surrounding discussion). In the heralded arm, the effect of loss is equivalent to convolution of the state Wigner function with a 2-dimensional Gaussian function, which blurs the peaks of any approximate GKP states being heralded.

In Fig. S14, we report the loss experienced by each mode in the experiment. There are several sources of losses that are common to all four modes: the resonator escape efficiency, waveguide propagation loss, and facet coupling loss. Escape efficiencies are measured by sweeping the frequency of a test laser and measuring the extinction of light coupled to the resonators. From this measurement, the resonator's escape efficiency, loaded quality factor, and (inferred) intrinsic quality factor are measured to be 0.974 (or 115 mdB loss), 3.33×10^5 and 1.28×10^7, respectively. The waveguide propagation loss includes all absorption, scattering, and radiation (due to waveguide bends) loss. This can be estimated from separate, component-level measurements. In total, this loss is determined to be $\sim$60 mdB. The facet coupling loss is determined from a loopback structure on the chip, where two neighbouring waveguides are coupled to each other through a loop, and is found to be $\sim$450 mdB.

There are also several sources of loss in this experiment that are not common to all modes. Mode 0 has two single-mode fiber splices in it, while modes 1,2 and 3 have three. Each splice is estimated to contribute $\sim$7 mdB of loss, calculated as an ensemble average from many splices. Mode 0 travels through a 50 m SMF28-Ultra fiber, experiencing $\sim$10 mdB of loss. Modes 1, 2 and 3 travel through 40 m of SMF28-e+ fiber, also experiencing $\sim$10 mdB of loss. Modes 1, 2 and 3 must go through a commercially available wavelength-demultiplexing (WDM) filter before reaching the PNR detectors. Each filter has a different measured loss in the range 231 mdB to 283 mdB. Modes 1, 2, and 3 reach three different PNR detectors. Their efficiencies, reported in sec. III, are measured in a separate experiment and correspond to between 5 mdB and 150 mdB. Finally, the detection loss experienced by mode 0 is estimated to be <130 mdB. This loss includes the photodiode quantum efficiency (>99%), 21.3 dB electronic noise clearance (99.3%), mode overlap between shaped LO pulse and quantum state

(>99%), and polarization visibility (>99%).

The squeezing resonators have several parasitic FWM processes that can generate photons in the mode of the squeezed state. First order parasitic FWM processes are imperfectly suppressed by the auxiliary resonator of the squeezer, while comb generation within the primary resonator enables second order FWM process as discussed in sec. I C. Since the contributions of these parasitic processes can be modeled as thermal states, their effect on squeezed vacuum can be equated with an effective loss. By solving the linear and nonlinear dynamics of the two coupled resonators via time domain coupled mode theory, this effective loss from parasitic FWM process is estimated by simulation to be ∼130 mdB.

In total, the loss experienced by Mode 0, 1, 2, and 3 are estimated to be 910 mdB, 1070 mdB, 1110 mdB, and 1170 mdB, respectively. These values are used to simulate the state presented in Fig. S18.

II. PHOTONIC CHIP FABRICATION, TESTING, AND DESIGN

A. Fabrication

All samples were fabricated on 300 mm wafers using a manufacturing process that is compatible with state-of-the-art, high-volume semiconductor manufacturing [10]. This process was customized and optimized specifically for application within this experiment. Fabrication begins with 300 mm silicon wafers, oxidized to produce a SiO2 layer that forms the bottom cladding for the silicon nitride (SiN) waveguides. SiN waveguides are fabricated using a subtractive process. Two SiN waveguiding layers are deposited, one with 400 nm thickness (used for the main functional components within the chip) and another with a thinner dimension used in conjunction with the 400 nm layer to facilitate efficient chip-fiber edge couplers. An SiO2 cladding layer vertically separates the two SiN layers. Taken together, the two SiN waveguide layers enable an edge coupler structure with <0.5 dB facet loss. The waveguide and cladding layers are processed with various treatments to reduce impurities, thereby reducing C-band propagation loss [11]. After fabrication of both waveguide levels, thermo-optic tuning elements were fabricated to enable optical phase shifters, including appropriate vias, electrical routing, and contacts for wire bonding. A photograph of a representative wafer is shown in Fig. S15.

B. Squeezer

The starting point of the squeezer design is a photonic molecule concept introduced in [3]. In this work we utilize SiN waveguides with 400 nm thickness to generate significant normal dispersion of ∼0.6 ps^2/m at 1550 nm (calculated through finite difference mode simulations and verified with measurements), a requirement to satisfy phase matching of the dual pump four-wave mixing (FWM) process in the presence of induced self- and cross-phase modulation [12]. To additionally suppress stimulated FWM processes from the two pumps, which would otherwise feed parasitic spontaneous FWM processes resulting in thermal photons being generated in the squeezing band, we strongly couple the two rings (peak splitting of primary resonances of approximately 10 GHz). The resulting dispersive effects from the phase response of the auxiliary rings resonances slightly push some of the primary ring resonances away from phase matching (due to symmetry, the pump resonances are unaffected). The nonlinear dynamics of the dual resonator system, including all the potential parasitic $\chi^{(3)}$ processes, were simulated with in-house software to determine the optimal coupling between the two resonators for the given waveguide geometry, as well as to determine the optimal pulsed pump conditions.

To attain the highest resonator quality factors with the 400 nm thickness, we utilized multi-mode waveguides (2.5 µm width), reducing scattering losses by a factor of five compared to single-mode geometry based on in-house simulations following the convention of [13]. The curvature of the waveguide bends in the coupling region and resonator were engineered to inhibit coupling to higher modes, through the use of parallelized finite difference time domain simulations running on the cloud using commercial software (Tidy3D from Flexcompute [14]).

FIG. S15: Example wafer. Photograph of a representative 300 mm wafer fabricated on the customized process used to yield chips for this experiment.

C. Beamsplitter

The operational range of 1545 nm to 1560 nm requires 50:50 beamsplitters with a relatively flat splitting ratio. As beamsplitters are used for filtering the pump beams as well as the base building blocks of the interferometer, they also require low insertion losses and fabrication tolerance. In this experiment, we utilize a design based on the wavelength insensitive coupler concept that uses a phase control region between a 50:50 and 100:0 coupler for a flat phase response [15, 16]. The fan-in/out waveguides were optimized to eliminate any excess bend loss or mode coupling effects. The splitting ratio was measured with grating coupled asymmetric Mach-Zehnder interferometer reference structures featured in each die. Averaged over the wavelength range 1545 to 1560 nm, the splitting ratio of the beamsplitter was measured to be >49.5% and the extinction ratio of a Mach-Zehnder interferometer was measured to be over 40 dB for 44 of 48 fields. The insertion loss of the beamsplitter was estimated as 4 mdB via loss racetrack structures [17].

D. Edge coupler

The edge coupler consists of a multi-layer design to enable highly efficient mode matching to medium mode field diameter (MFD) fiber (6.4 µm MFD, Corning HI 1060 Flex) [18]. The coupled waveguide geometry is highly tolerant to fabrication variation, with a deviation of 20 nm leading to an excess loss of only 25 mdB. The mode is adiabatically transformed, through the use of multiple tapers, from the edge coupling region to the single mode routing waveguide of 1 µm width. The design maintains significant spacing between all waveguides, preventing the potential impact of voids in the oxide often present in subtractive SiN photonics flows [19].

E. Packaging

The 300 mm wafers were singulated using a custom optical grade dicing process at a commercial dicing facility. The edge couplers on the diced chips containing the circuits were qualified with monitor

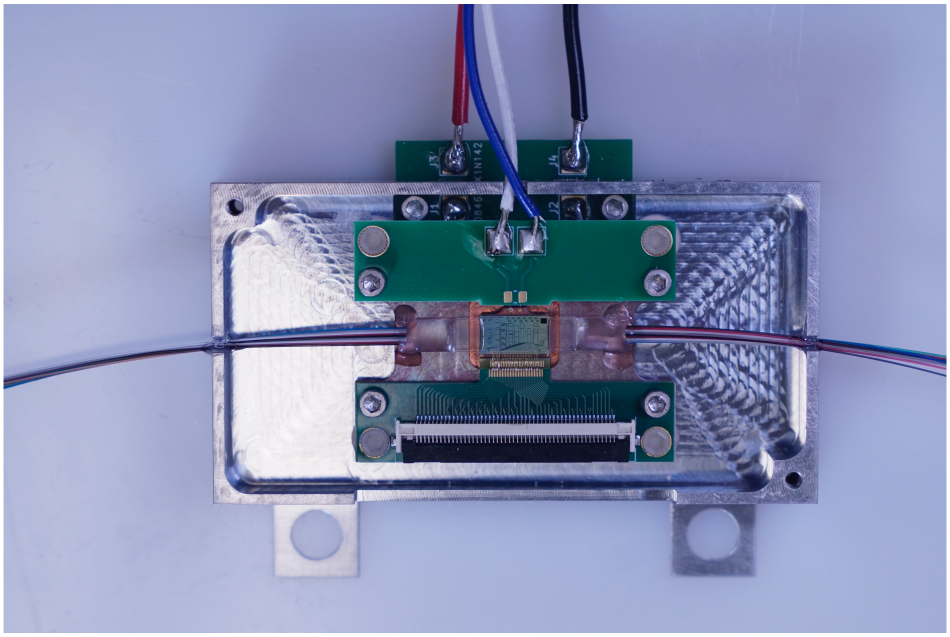

FIG. S16: Electrically and optically packaged chip. The chip is optically packaged to two fiber arrays, electrically packaged by wirebonding to a PCB, and thermally stabilized using a thermoelectric cooler.

structures with an in-house low loss measurement setup (± 0.01 dB precision), with 28 fields obtaining through-chip transmission of <0.5 dB including both input and output coupling losses. Upon down-selection, the dies were briefly polished, typically removing approximately 5 µm to improve surface quality, followed by further inspection of facet angles. The chip and thermistor were die bonded onto a copper sub mount followed by wirebonding using semi-automatic hardware. Custom fiber arrays consisting of HI 1060 Flex fiber (MFD of 6.4 µm) were attached in-house using optimized processes on a standard commercial system (Ficontec A-300). The packaged arrays underwent strain-relief and were accessed with SMF28 Ultra fiber, with a typical splice loss of $\sim$0.1 dB to HI 1060 Flex. A photograph of the chip in the enclosure is shown in Fig. S16.

III. PHOTON NUMBER RESOLVING DETECTORS

The three photon-number resolving (PNR) detectors, based on transition edge sensors (TES), used in this experiment have directly measured detection efficiencies (DE) of $99.89^{+0.11}_{-0.53}\%$, $98.40 \pm 1.19\%$, and $96.45 \pm 1.04\%$, where uncertainties represent a 95% confidence interval ($k = 2$). The primary contributor to these uncertainties is the absolute calibration of the optical power meter, which has an uncertainty of 0.42% ($k = 2$). This calibration was performed by metrologists at NIST. The next most significant factor is the photon statistical error, which is influenced by the signal-to-noise ratio of each detector. This variation in signal-to-noise ratio is also the primary reason the uncertainties differ across the three channels.

Multiple additional detectors in our TES fabrication run for this experiment were yielded that showed measured detection efficiencies above 99%. That two sensors with slightly lower detection efficiency were used in this experiment is the outcome of a selection procedure that balances the electrical noise properties with the optical detection efficiency. The electronic properties are related to the electronic packaging process, which requires careful assembly to enable faithful readout of the small electrical signals produced by each sensor. This assembly process has not yet been fully optimized, and is not correlated with detection efficiency. The primary cause of the variation in the detection efficiency for the samples used stems from the manual fiber assembly process, which leads to variations in the alignment of the optical fiber tips relative to the sensor area. Improvements in the optical and electronic assembly process are expected to result in a supply of PNR detectors with reliably $> 99\%$ DE.

Accurate measurement of DE requires a well-calibrated optical power meter (OPM) and precisely characterized variable optical attenuators (VOAs). Calibration was conducted by the Optical Fiber Power Metrology Group at NIST Boulder, Colorado, in June 2024. We employed a variant of the multiple attenuator method, previously used for TES [20] and Superconducting Nanowire Single-Photon Detectors (SNSPD) [21, 22] in DE measurements.

Reliable DE characterization necessitates that the VOAs exhibit linear, repeatable attenuation and the OPM must have absolute calibration at two power levels. Additionally, the OPM was calibrated for nonlinearity and range-boundary discontinuities adding to the uncertainty budget. Both continuous-wave (CW) and pulsed laser light were used; CW light for VOA and switch-ratio characterizing VOA and pulsed light for reference measurements and photon counting.

The experimental setup included a 2×1 optical switch for source selection, followed by a polarization scrambler, three VOAs, and a 1×2 switch directing outputs to calibrated OPMs. The pulsed laser was measured at $\sim 10\,\mu\text{W}$, aligning with an OPM calibration point, requiring $\sim 90\,\text{dB}$ of total attenuation (30 dB per VOA) to achieve an average photon number of 1 (per pulse). CW light was used to measure each VOA's attenuation, first recording a 0 dB reference, then setting each VOA to 30 dB and measuring the output power. The 1×2 switch ratio, S, was calibrated by measuring the power at each OPM 100 times. After CW measurements, the pulsed laser was input to measure the reference power, P_0 (again $\sim 10\,\mu\text{W}$). The expected power after attenuation was calculated as

$$P_{\text{expected}} = P_0 S \alpha_1 \alpha_2 \alpha_3 \tag{3}$$

where the α_1, α_2, and α_3 values represent the VOA attenuation factors. One million output traces were acquired from the TES and analysed using principal component analysis (PCA) [23, 24] to determine the average photon number $\bar{n}$ with associated uncertainties. The measured power, P_{measured}, was determined by

$$P_{\text{measured}} = \bar{n} E R \, , \tag{4}$$

where E is the energy of a photon at 1545.32 nm, and R is the repetition rate of the pulsed laser. The detection efficiency is then

$$\text{DE} = \frac{P_{\text{measured}}}{P_{\text{expected}}} \, . \tag{5}$$

IV. THEORY

A. GBS architecture and simulation

Gaussian Boson Sampling (GBS) state preparation devices are probabilistic sources of non-Gaussian states. They deterministically prepare a multimode entangled Gaussian state and then measure a subset of those modes with photon-number resolving measurements (PNRs), resulting in output states being heralded in the remaining unmeasured modes [9, 25–31]. Desired target states can be generated by appropriate tuning of the parameters of the Gaussian state, and by conditioning on specific PNR patterns. Previous theoretical works have studied GBS devices as sources of approximate GKP states [9, 26, 28, 30, 31], with this experiment providing validation of the approach.

Background theory and derivations for the "staircase" GBS architecture used in the device presented here can be found in Section IV of the supplementary material of Ref. [9]. The quantum optical circuit can be found in Fig. S17. In summary, the device architecture was derived by first considering an optical circuit that generates GKP states by taking approximate squeezed cat states generated by 2-mode GBS devices [29] and breeding them together via beamsplitter interactions and generaldyne measurements (projections onto squeezed coherent states). The latter is a generalization of the breeding protocol

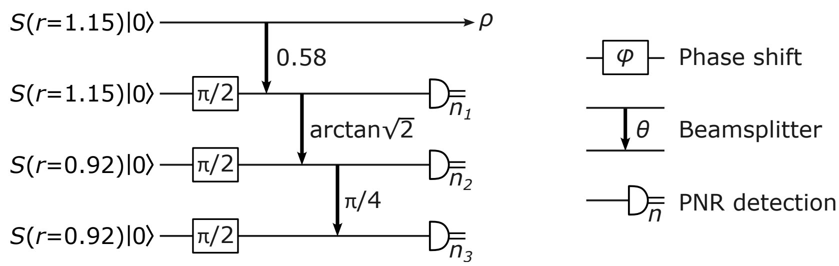

FIG. S17: Diagram of circuit implementation. Quantum optical circuit for the four-mode "staircase" GBS circuit, including the squeezing and interferometer settings that were targeted in the experiment. The conventions for optical elements can be found in the documentation for Mr-Mustard [36].

with homodyne detection [32–35]. Considering the complete optical circuit comprised of Gaussian states, PNR measurements and generaldyne measurements, all the generaldyne measurements can be applied to the multimode entangled Gaussian state first, which maps the remaining modes to a smaller multimode Gaussian state. Then, we can instead consider a GBS device with fewer modes that prepares that resulting smaller multimode Gaussian state directly. By construction, applying the PNR measurements to that Gaussian state will generate the same output states as the larger optical circuit that included generaldyne measurements. The case of three 2-mode GBS devices and two generaldyne measurements maps to the 4-mode GBS device architecture used in this experiment.

To simulate the optical circuits of the GBS devices, we use MrMustard [36]. Because the unitary in the GBS device (see Fig. S3) is not universal and the first mode is only directly coupled via beamsplitter to the second mode before the second mode is coupled to the remaining modes, we can treat the last two beamsplitters and the three PNR measurements as an effective POVM that acts on the second mode of the circuit. We employ the Fock-Bargmann representation to describe the Gaussian state in the first two modes, and to compute the inner product between the second mode and the effective POVM, we use the Fock basis. We employed simulations to determine which squeezing and beamsplitter settings to use for the experiment, optimizing $\min(\Delta_p^2, \Delta_q^2)$ to be as large as possible (in dB units with higher squeezing being larger, see Methods) given the levels of loss in the experiment. In Fig. S18(left), we show a simulated Wigner function for the state heralded by the $(3, 3, 3)$ PNR outcome that includes both loss and Schmidt modes; it has 97.8% fidelity to the state from the experiment. Here, we assume effective transmissions of (81.1%, 80.6%, 79.8%, 78.8%) in each mode, input squeezing levels of (10, 10, 8, 8) dB, and beamsplitter angles of (0.58, $\arctan\sqrt{2}$, $\pi/4$). The first squeezer has a phase of $\pi/2$ relative to the others. Additionally, we simulate two temporal modes for each spatial mode such that the Schmidt number is $K = 1.12$; since these two sets of modes are decoupled, we can simulate them independently then take mixtures of all possible combinations of outcomes in the temporal modes that yield PNR pattern $(3, 3, 3)$ in the three spatial modes, since the PNR detectors cannot distinguish between temporal modes. There are likely additional imperfections in the experimental setup which we have not characterized, such as PNR detector miscategorization and thermal noise in the squeezed states which account for the difference between simulation and experiment. In Fig. S18(right), we also provide a simulation for the state in the case where loss is the only imperfection, and find a fidelity of 94.9% to the state in the experiment. The same simulation technique was used to produce the data for Fig. 4 of the main text, with the simplification that we only considered one temporal mode per spatial mode, and optimized for symmetric effective squeezing in the lossless case.

As discussed in the main text, in addition to needing lower photon loss, the path to deterministic generation of high-quality GKP generation, as presented in Ref. [9, 35], is to employ higher input squeezing, to accept more PNR outcomes from the GBS devices, and to apply multiplexing and adaptive breeding protocols to the output states of GBS devices with fewer modes. Table I and Fig. 3d in Ref. [35] show that an order of magnitude boost in success probability can be achieved by increasing the input squeezing to the GBS devices and by accepting more PNR outcomes. Fig. S12b in Ref. [9] shows that the cumulative success probability of the "staircase" GBS device producing states

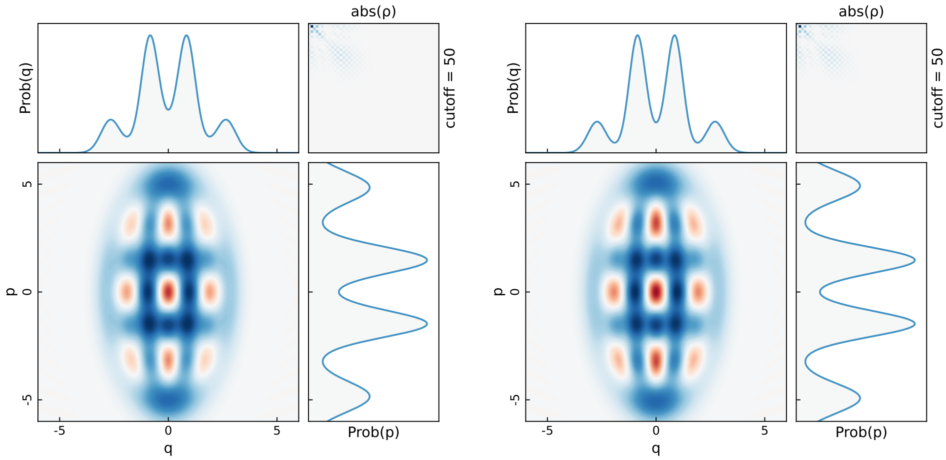

FIG. S18: Simulated Wigner function for the state heralded by (3,3,3) (*left*) with 97.8% fidelity to the state from the experiment when including the measured losses and Schmidt number of the experiment, and (*right*) with 94.9% fidelity when only including the measured losses but no extra Schmidt modes. See text for simulation parameters.

that can be bred into high quality GKP states increases by roughly an order of magnitude were one to switch from a four-mode device to a three-mode device, and an order of magnitude further if one considers a two-mode device.

B. Effective squeezing for Gaussian pure states

In Section II.B of the supplementary material of Ref. [9] and in Ref. [37], it is shown that stabilizer expectation values are invariant under a Gaussian unitary $\hat{U}_G$ as long as the corresponding transformation $\hat{U}_G^\dagger$ is applied to the lattice defined by the stabilizers. Therefore, to determine the best symmetric effective squeezing for Gaussian pure states, it is sufficient to fix a Gaussian pure state, then optimize over choices of lattice defined by the stabilizers, since all lattices are related to each other by Gaussian unitaries [38]. If we fix the vacuum state and optimize over possible choices of stabilizers, we find that $\hat{S}_q = e^{i\sqrt{2\pi}\hat{q}}$, $\hat{S}_p = e^{i\sqrt{2\pi}\hat{p}}$ is the optimal choice, yielding simultaneous stabilizer expectation values $|\langle 0|\hat{S}_q|0\rangle| = |\langle 0|\hat{S}_p|0\rangle| \approx 0.208$.

C. Effective squeezing vs. stellar rank

A non-Gaussian pure state can always be written as $\hat{U}_G \sum_{n=0}^{N} c_n |n\rangle$, where $\hat{U}_G$ is a Gaussian unitary, $|n\rangle$ are Fock states, and N is the stellar rank [39]. As discussed in the main text, high stellar rank is necessary for producing approximate GKP states with high symmetric effective squeezing. As a simple numerical experiment using `scipy.optimize`, we optimize over $\hat{U}_G$, and the coefficients c_n to find the highest symmetric effective squeezing as a function of N. The results in Fig. S19 show that there is a state with stellar rank $N = 18$ that is able to surpass symmetric effective squeezing of 9.75 dB.

The output states of GBS devices have stellar rank at most equal to the number of photons detected by the PNRs [26]. The states from Fig. 4 of the main text which can achieve symmetric effective squeezing greater than 9.75 dB have $N \geq 24 = 8 + 8 + 8$, consistent with what is sufficient from Fig. S19. Based on the agreement between simulation and experiment for our device, were losses reduced

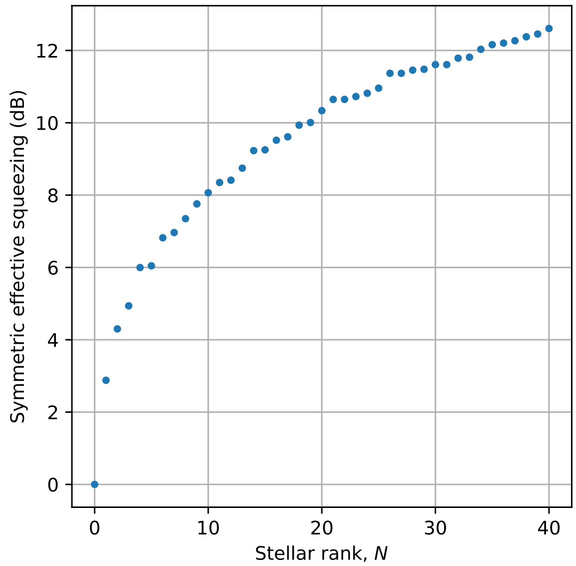

FIG. S19: Optimized symmetric effective squeezing vs. stellar rank

further, the $(3, 3, 3)$ outcome would have stellar rank 9.

---

[1] V. Vaidya and Z. Yanbing, Methods and systems for pulsed beam phase locking (2023), uS Patent App. 17/827,929.

[2] R. W. P. Drever, J. L. Hall, F. V. Kowalski, J. Hough, G. M. Ford, A. J. Munley, and H. Ward, Laser phase and frequency stabilization using an optical resonator, Applied Physics B **31**, 97 (1983).

[3] Y. Zhang, M. Menotti, K. Tan, V. D. Vaidya, D. H. Mahler, L. G. Helt, L. Zatti, M. Liscidini, B. Morrison, and Z. Vernon, Squeezed light from a nanophotonic molecule, Nature Communications **12**, 2233 (2021).

[4] Z. Qin, A. S. Prasad, T. Brannan, A. MacRae, A. Lezama, and A. I. Lvovsky, Complete temporal characterization of a single photon, Light: Science & Applications **4**, e298 (2015).

[5] A. Christ, K. Laiho, A. Eckstein, K. N. Cassemiro, and C. Silberhorn, Probing multimode squeezing with correlation functions, New Journal of Physics **13**, 033027 (2011).

[6] Z. Vernon, N. Quesada, M. Liscidini, B. Morrison, M. Menotti, K. Tan, and J. Sipe, Scalable squeezed-light source for continuous-variable quantum sampling, Phys. Rev. Appl. **12**, 064024 (2019).

[7] J. B. Christensen, J. G. Koefoed, K. Rottwitt, and C. J. McKinstrie, Engineering spectrally unentangled photon pairs from nonlinear microring resonators by pump manipulation, Opt. Lett. **43**, 859 (2018).

[8] A. I. Lvovsky, Iterative maximum-likelihood reconstruction in quantum homodyne tomography, J. Opt. B: Quantum Semiclass. Opt. **6**, S556 (2004).

[9] H. Aghaee Rad, T. Ainsworth, R. Alexander, B. Altieri, M. Askarani, R. Baby, L. Banchi, B. Baragiola, J. Bourassa, R. Chadwick, *et al.*, Scaling and networking a modular photonic quantum computer, Nature 10.1038/s41586-024-08406-9 (2025).

[10] D. J. Blumenthal, R. Heideman, D. Geuzebroek, A. Leinse, and C. Roeloffzen, Silicon nitride in silicon photonics, Proceedings of the IEEE **106**, 2209 (2018).

[11] M. H. P. Pfeiffer, J. Liu, A. S. Raja, T. Morais, B. Ghadiani, and T. J. Kippenberg, Ultra-smooth silicon nitride waveguides based on the damascene reflow process: fabrication and loss origins, Optica **5**, 884 (2018).

[12] Y. Okawachi, M. Yu, K. Luke, D. O. Carvalho, S. Ramelow, A. Farsi, M. Lipson, and A. L. Gaeta, Dual-pumped degenerate kerr oscillator in a silicon nitride microresonator, Opt. Lett. **40**, 5267 (2015).

[13] T. Barwicz and H. Haus, Three-dimensional analysis of scattering losses due to sidewall roughness in microphotonic waveguides, Journal of Lightwave Technology **23**, 2719 (2005).

[14] T. W. Hughes, M. Minkov, V. Liu, Z. Yu, and S. Fan, A perspective on the pathway toward full wave

simulation of large area metalenses, Applied Physics Letters **119**, 150502 (2021).

[15] K. Jinguji, N. Takato, A. Sugita, and M. Kawachi, Mach–zehnder interferometer type optical waveguide coupler with wavelength-flattened coupling ratio, Electronics Letters **26**, 1326 (1990).

[16] M. Cherchi, The bloch sphere: a powerful tool to design photonic integrated circuits, in *Optica Advanced Photonics Congress 2022* (Optica Publishing Group, 2022) p. ITu3B.2.

[17] A. M. Jones, C. T. DeRose, A. L. Lentine, A. Starbuck, A. T. Pomerene, and R. A. Norwood, Racetrack resonator as a loss measurement platform for photonic components, Opt. Express **23**, 28883 (2015).

[18] I. Krasnokutska and B. Morrison, Apparatus for optical coupler (2024), uS Patent App. 18/518,746.

[19] M. H. P. Pfeiffer, C. Herkommer, J. Liu, T. Morais, M. Zervas, M. Geiselmann, and T. J. Kippenberg, Photonic damascene process for low-loss, high-confinement silicon nitride waveguides, IEEE Journal of Selected Topics in Quantum Electronics **24**, 1 (2018).

[20] A. J. Miller, A. E. Lita, B. Calkins, I. Vayshenker, S. M. Gruber, and S. W. Nam, Compact cryogenic self-aligning fiber-to-detector coupling with losses below one percent, Opt. Express **19**, 9102 (2011).

[21] F. Marsili, V. Verma, J. Stern, S. Harrington, A. Lita, T. Gerrits, I. Vayshenker, B. Baek, M. Shaw, R. Mirin, and S. W. Nam, Detecting single infrared photons with 93 % system efficiency, Nature Photonics **7**, 210 (2013).

[22] D. V. Reddy, R. R. Nerem, S. W. Nam, R. P. Mirin, and V. B. Verma, Superconducting nanowire single-photon detectors with 98% system detection efficiency at 1550nm, Optica **7**, 1649 (2020).

[23] E. Figueroa-Feliciano, B. Cabrera, A. Miller, S. Powell, T. Saab, and A. Walker, Optimal filter analysis of energy-dependent pulse shapes and its application to tes detectors, Nuclear Instruments and Methods in Physics Research Section A **444**, 453 (2000).

[24] P. C. Humphreys, B. J. Metcalf, T. Gerrits, T. Hiemstra, A. E. Lita, J. Nunn, S. W. Nam, A. Datta, W. S. Kolthammer, and I. A. Walmsley, Tomography of photon-number resolving continuous-output detectors, New Journal of Physics **17**, 103044 (2015).

[25] K. K. Sabapathy, H. Qi, J. Izaac, and C. Weedbrook, Production of photonic universal quantum gates enhanced by machine learning, Phys. Rev. A **100**, 012326 (2019).

[26] D. Su, C. R. Myers, and K. K. Sabapathy, Conversion of gaussian states to non-gaussian states using photon-number-resolving detectors, Phys. Rev. A **100**, 052301 (2019).

[27] N. Quesada, L. G. Helt, J. Izaac, J. M. Arrazola, R. Shahrokhshahi, C. R. Myers, and K. K. Sabapathy, Simulating realistic non-gaussian state preparation, Phys. Rev. A **100**, 022341 (2019).

[28] I. Tzitrin, J. E. Bourassa, N. C. Menicucci, and K. K. Sabapathy, Progress towards practical qubit computation using approximate Gottesman-Kitaev-Preskill codes, Phys. Rev. A **101**, 032315 (2020).

[29] K. Takase, J.-i. Yoshikawa, W. Asavanant, M. Endo, and A. Furusawa, Generation of optical Schrödinger cat states by generalized photon subtraction, Phys. Rev. A **103**, 013710 (2021).

[30] K. Fukui, S. Takeda, M. Endo, W. Asavanant, J.-i. Yoshikawa, P. van Loock, and A. Furusawa, Efficient backcasting search for optical quantum state synthesis, Phys. Rev. Lett. **128**, 240503 (2022).

[31] K. Takase, K. Fukui, A. Kawasaki, W. Asavanant, M. Endo, J.-i. Yoshikawa, P. van Loock, and A. Furusawa, Gottesman-Kitaev-Preskill qubit synthesizer for propagating light, npj Quantum Information **9**, 98 (2023).

[32] H. M. Vasconcelos, L. Sanz, and S. Glancy, All-optical generation of states for "encoding a qubit in an oscillator", Optics Letters **35**, 3261 (2010).

[33] D. J. Weigand and B. M. Terhal, Generating grid states from Schrödinger-cat states without postselection, Phys. Rev. A **97**, 022341 (2018).

[34] M. Eaton, R. Nehra, and O. Pfister, Non-gaussian and gottesman–kitaev–preskill state preparation by photon catalysis, New J. Phys. **21**, 113034 (2019).

[35] K. Takase, F. Hanamura, H. Nagayoshi, J. E. Bourassa, R. N. Alexander, A. Kawasaki, W. Asavanant, M. Endo, and A. Furusawa, Generation of flying logical qubits using generalized photon subtraction with adaptive gaussian operations, Physical Review A **110**, 012436 (2024).

[36] XanaduAI, MrMustard, `https://github.com/XanaduAI/MrMustard` (2021).

[37] P. Marek, Ground state nature and nonlinear squeezing of gottesman-kitaev-preskill states, Phys. Rev. Lett. **132**, 210601 (2024).

[38] D. Gottesman, A. Kitaev, and J. Preskill, Encoding a qubit in an oscillator, Phys. Rev. A **64**, 012310 (2001).

[39] U. Chabaud, D. Markham, and F. Grosshans, Stellar representation of non-gaussian quantum states, Phys. Rev. Lett. **124**, 063605 (2020).

Appendix A: Heralded state zoo

Below figures shows Wigner functions of all heralded states with heralding pattern ($n_1 \leq 5, n_2 \leq 5, n_3 \leq 5$). Upper-left corner of each plot shows the heralding pattern, while upper-right corner shows the number of quadrature measurements used in the state reconstruction. Note, some of the states are reconstructed from a small dataset of only few 100k quadrature measurements, causing the Wigner function to by noisy and uncertain. $\hbar = 1$ is used.

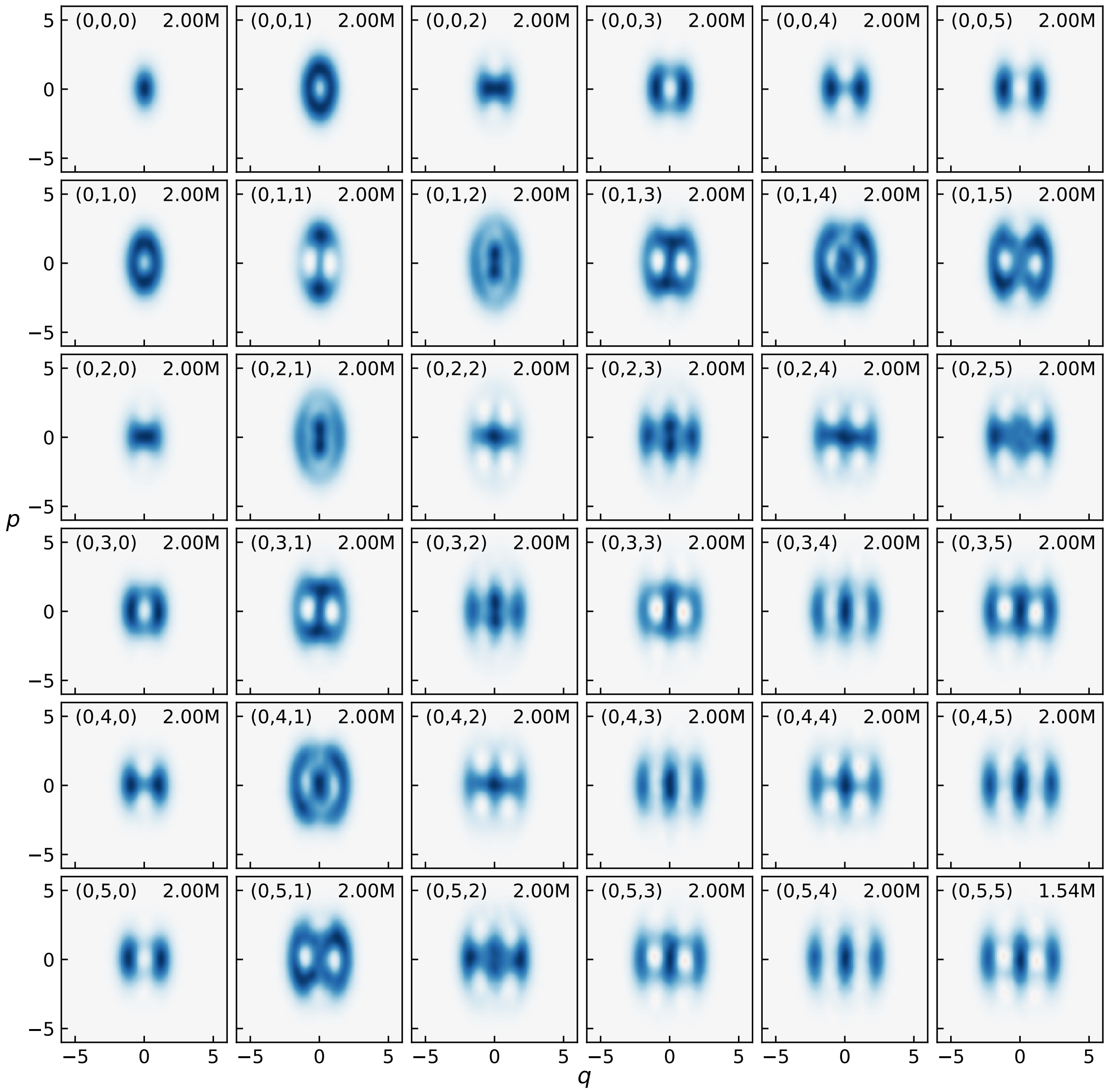

FIG. S20: Wigner functions of heralded states, here with heralding pattern ($n_1 = 0, n_2, n_3$).

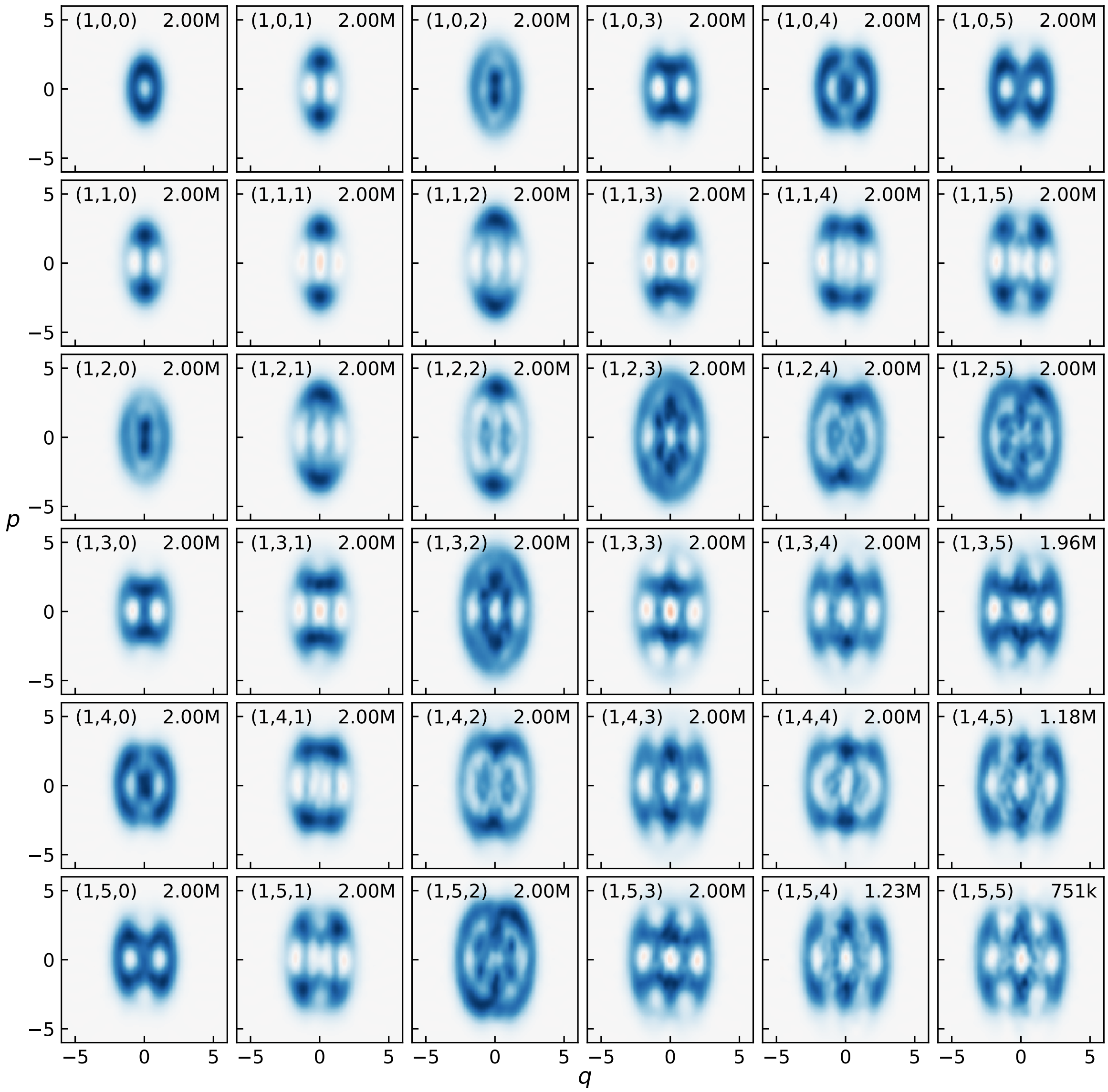

FIG. S21: Wigner functions of heralded states, here with heralding pattern $(n_1 = 1, n_2, n_3)$.

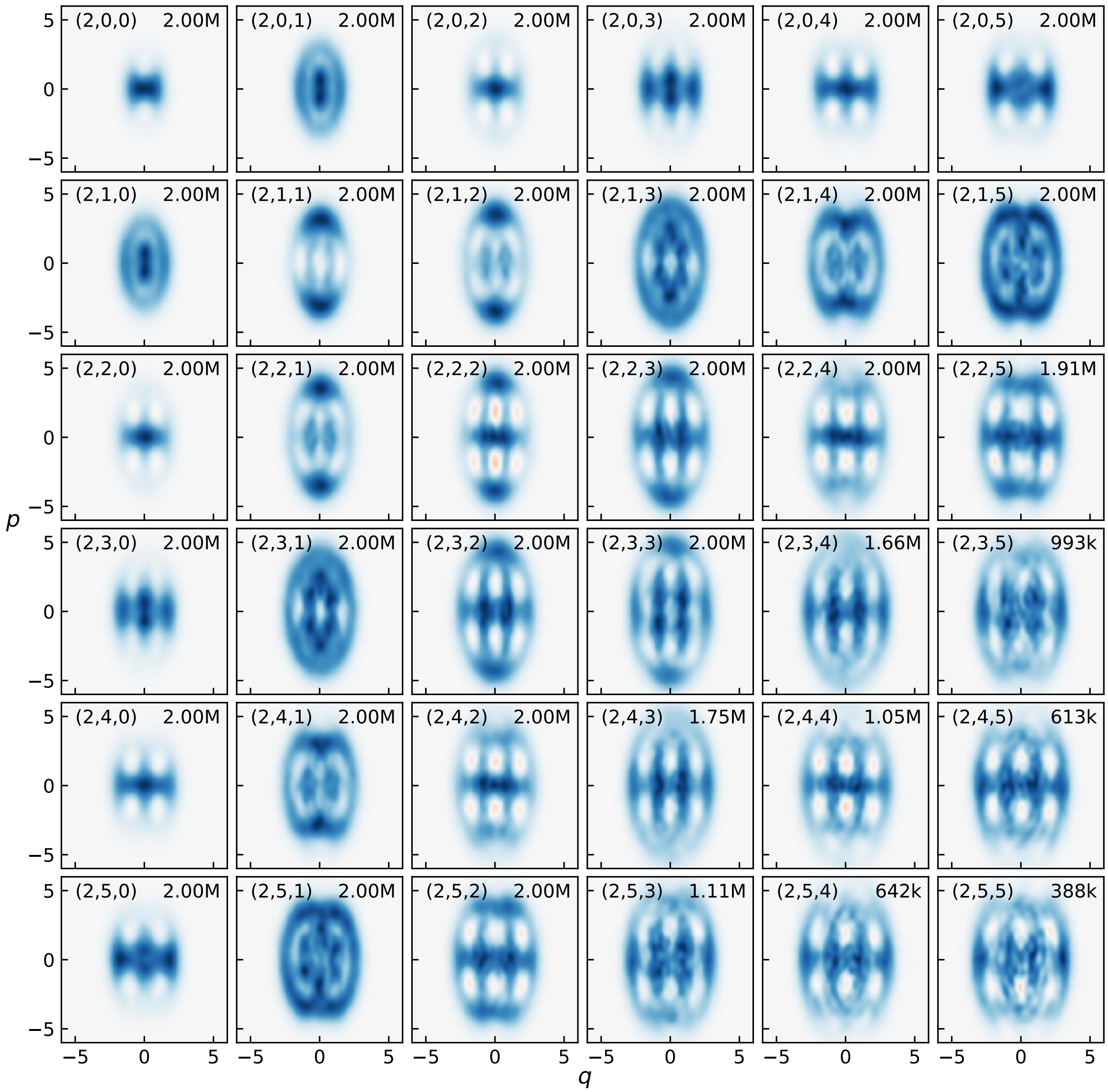

FIG. S22: Wigner functions of heralded states, here with heralding pattern $(n_1 = 2, n_2, n_3)$.

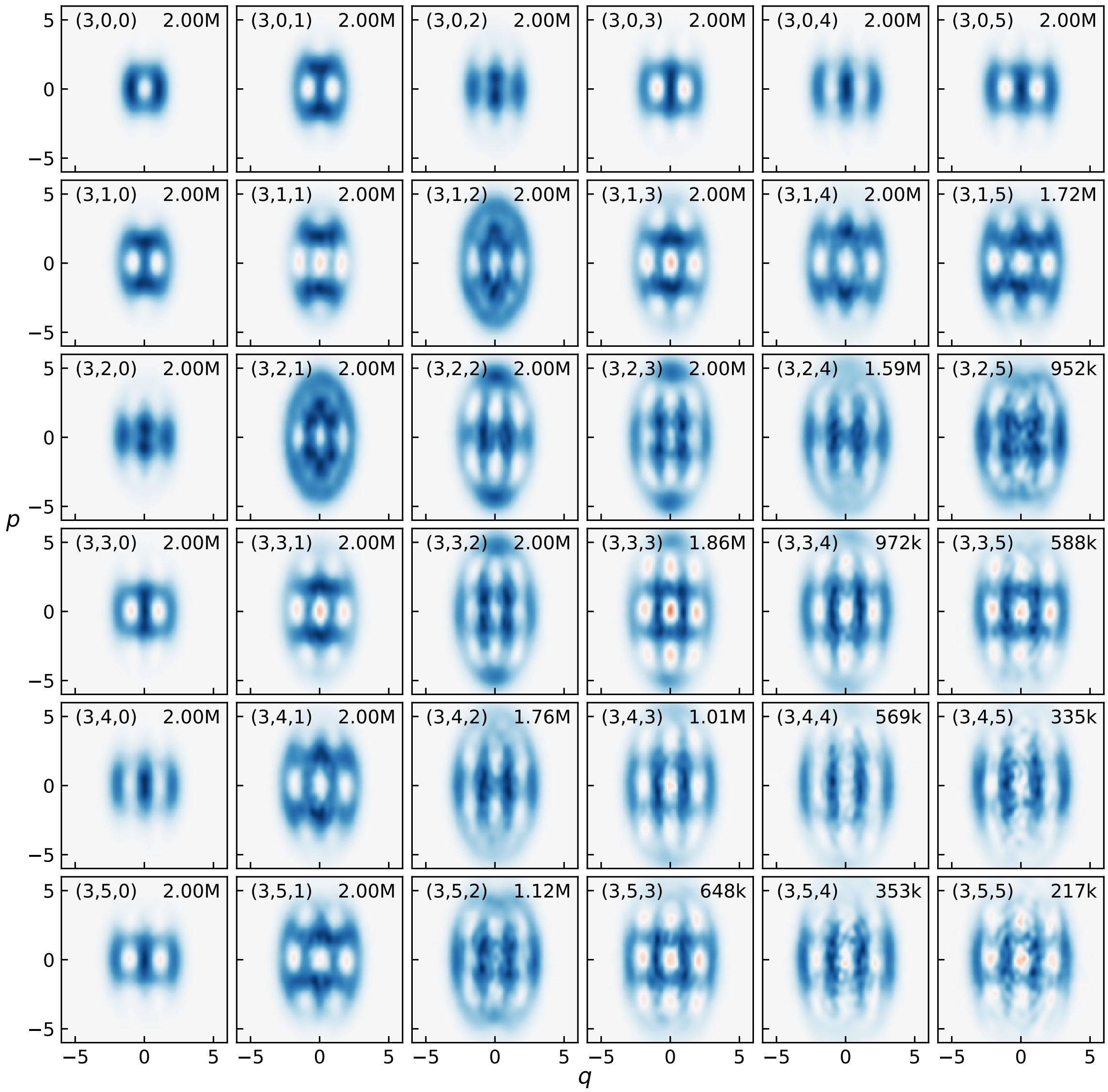

FIG. S23: Wigner functions of heralded states, here with heralding pattern $(n_1 = 3, n_2, n_3)$.

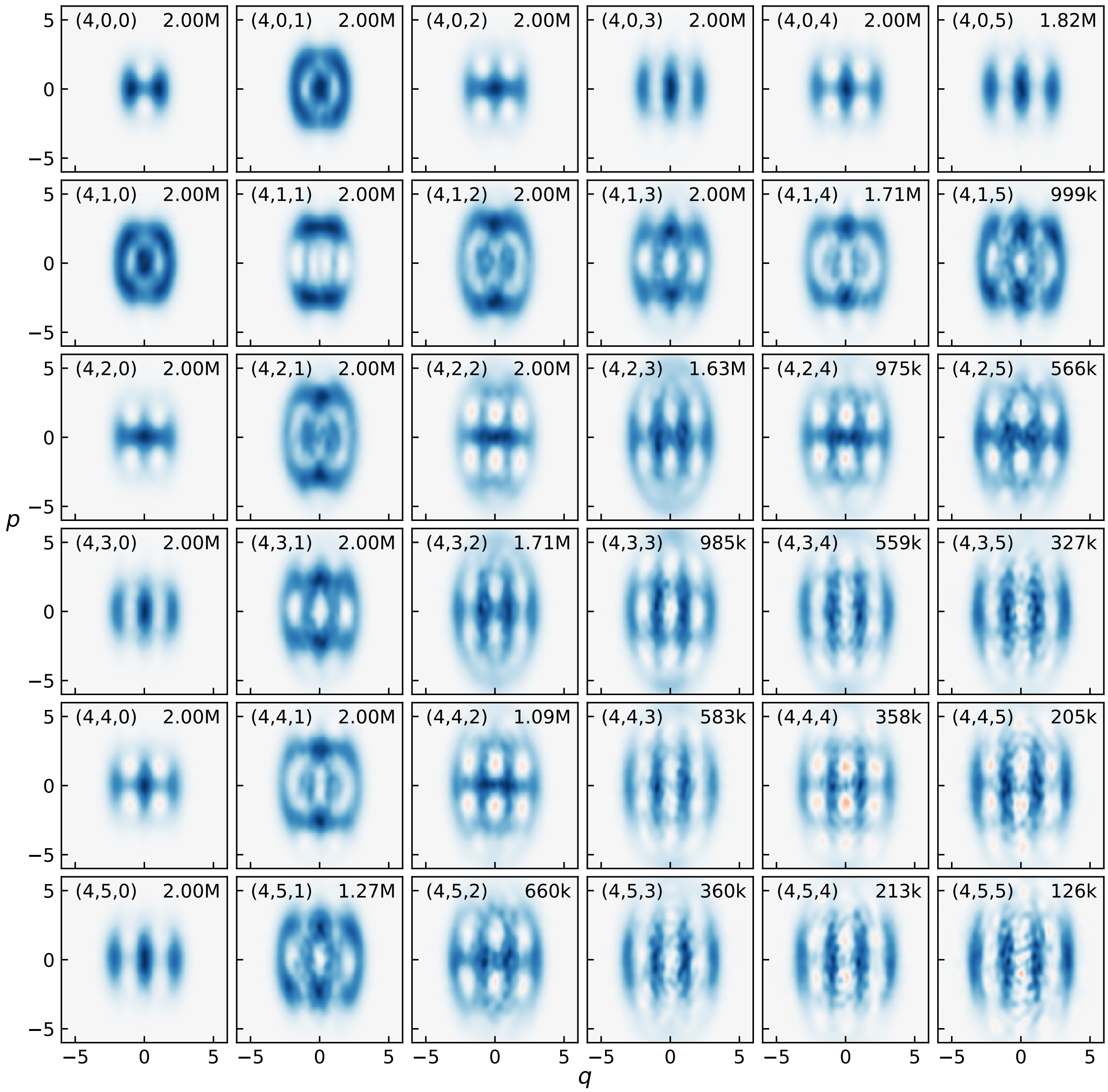

FIG. S24: Wigner functions of heralded states, here with heralding pattern $(n_1 = 4, n_2, n_3)$.

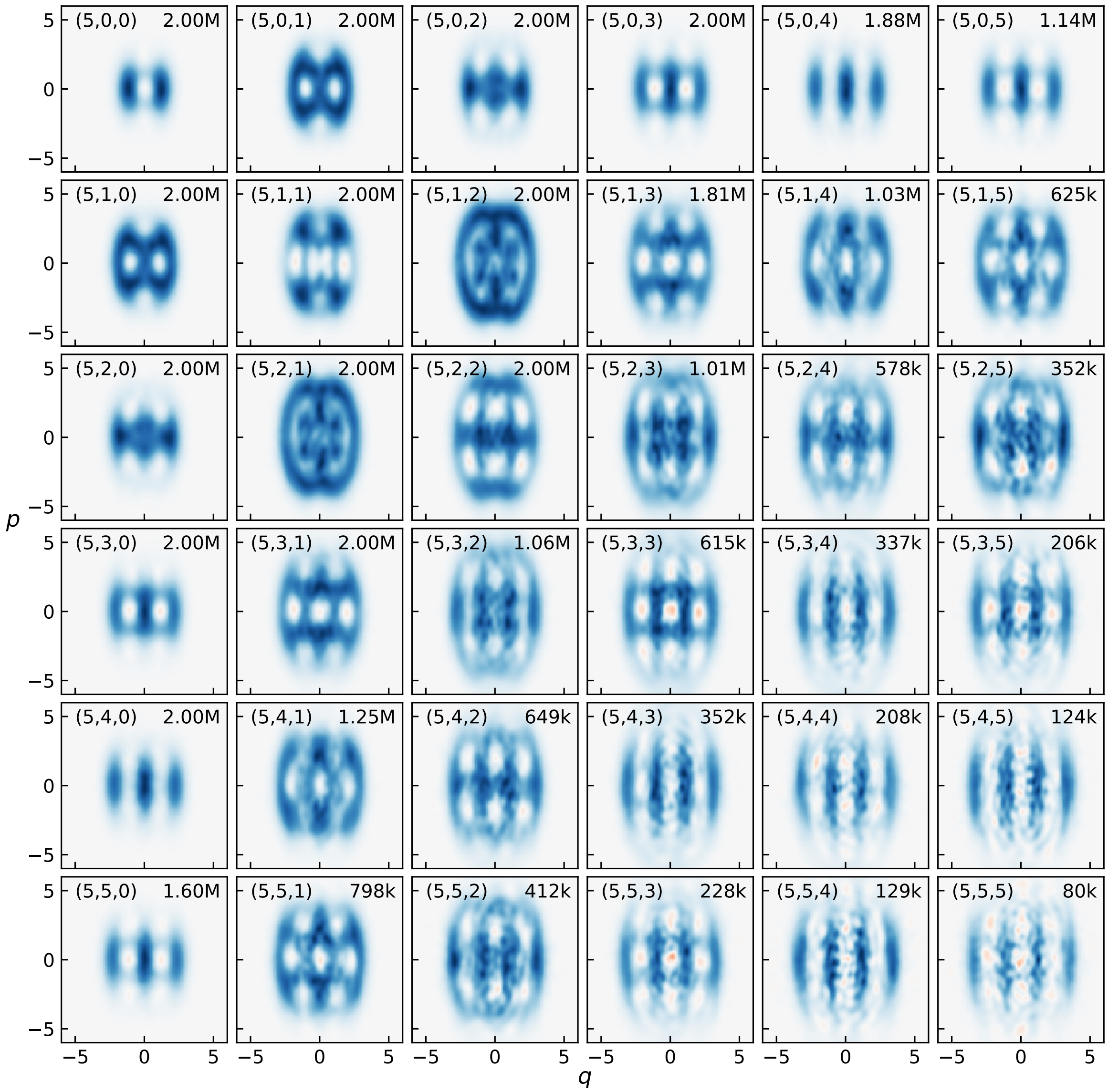

FIG. S25: Wigner functions of heralded states, here with heralding pattern $(n_1 = 5, n_2, n_3)$.